Open Access

Advances in Environmental and Engineering Research

LIDSEN Publishing Inc.

Original Research

Kinetic Modelling, Faraday-Based Continuous-Flow Projection, and Techno-Economic Assessment of Electrocoagulation-Filtration for Batik Wastewater

Erina Rahmadyanti [1, *], Danayanti Azmi Dewi Nusantara [1], Ronny Durrotun Nasihien [2], Dimas Nur Prakoso [3], Sugeng Rifqi Mubaroq [4]

1. Department of Civil Engineering, Faculty of Engineering, Universitas Negeri Surabaya, Ketintang, Surabaya 60231, Indonesia; E-Mails: erinarahmadyanti@unesa.ac.id; danayantinusantara@unesa.ac.id; ORCID: 0000-0002-8055-717X; 0009-0003-0249-7735
2. Department of Civil Engineering, Faculty of Engineering, Universitas Narotama, Sukolilo, Surabaya 60117, Indonesia; E-Mail: ronny.durrotun@narotama.ac.id; ORCID: 0000-0003-2915-7602
3. Vocational Program of Electrical Engineering, Politeknik Negeri Madiun, Taman, Madiun 63151, Indonesia; E-Mail: dimasnur@pnm.ac.id; ORCID: 0009-0007-8410-9888
4. Technical and Vocational Education Study Program, Sekolah Pascasarjana, Universitas Pendidikan Indonesia, Bandung 40154, Indonesia; E-Mail: mubaroq@upi.edu; ORCID: 0000-0001-8933-5867

* **Correspondence:** Erina Rahmadyanti; E-Mail: erinarahmadyanti@unesa.ac.id; ORCID: 0000-0002-8055-717X

Academic Editor: Md Tabish Noori

Adv Environ Eng Res
2026, volume 7, issue 3
doi:10.21926/aeer.2603022

Received: April 20, 2026
Accepted: June 29, 2026
Published: July 21, 2026

Abstract

Wastewater from stamped batik (*batik cap*) — the block-printing method that dominates micro, small, and medium enterprise (MSME) production across Southeast Asia — is commonly discharged without a transferable design basis for continuous-flow scale. This study links batch-scale electrocoagulation-filtration (EC-F) kinetics to operational current-density projections for a 1 m^3/day wastewater treatment plant, complemented by techno-economic and carbon footprint assessments. A 2 × 3 factorial batch experiment with

aluminium electrodes was conducted on real batik cap effluent. Six candidate kinetic forms — exponential saturation, pseudo-first-order, pseudo-second-order, Langmuir-hyperbolic, Gompertz, and logistic — were compared via AIC; sigmoidal forms (Gompertz at 4 cm gap; logistic at 2 cm gap) provided substantially better description of the η versus Faraday aluminium-dose data than the exponential baseline (ΔAIC = 5–38). The spacing factor was retained after controlling for total charge as a covariate (ANCOVA $p < 10^{-4}$ for all three parameters), confirming a genuine geometric-mass-transfer effect beyond the coulombic load. The laboratory optimum yielded chemical oxygen demand, biochemical oxygen demand, and total suspended solids removals above 92% at a specific energy demand of 4.5-10.5 kWh kg^{-1} pollutant. The continuous-flow projection — explicitly framed as a predictive scale-up framework rather than a validated solution — recommends an operational current density of ≈1.4 mA cm^{-2} (parameter-wise medians 1.28-1.36 mA cm^{-2}; combined safety value 1.4), one order of magnitude below the batch range, with projected effluent compliant with national discharge standards. Operational cost of USD 1.05-1.75 m^{-3} (correlated Monte Carlo, n = 20,000) is most sensitive to the kinetic rate constant and the aluminium plate price; the carbon footprint is dominated by primary aluminium production (89% of 10.4 kg CO_2 m^{-3}) and can be reduced to 0.99 kg CO_2 m^{-3} by combining recycled-aluminium electrodes with photovoltaic power. A trade-off analysis between removal efficiency and sludge generation is also reported. The framework provides an auditable, MSME-relevant design basis for EC scale-up in the Southeast Asian batik sector.

Keywords
Electrocoagulation; batik cap wastewater; kinetic modelling; Faraday scale-up; techno-economic assessment; carbon footprint

1. Introduction

The textile sector is among the most water- and chemical-intensive industries worldwide, generating heavily coloured effluents with high organic loads and persistent synthetic dyes [1, 2]. In developing countries, particularly across Southeast Asia, most actors in this sector are traditional micro, small, and medium enterprises (MSMEs) scattered beyond the reach of centralised wastewater treatment plants (WWTPs), so that their effluents are commonly discharged without adequate treatment [3, 4].

A notable representative of the MSME textile sector is batik, a wax-resist cloth-dyeing craft rooted in the traditions of Indonesia and Malaysia, with strategic economic and cultural roles. Batik is produced by three methods distinguished by how wax is applied: hand-drawn (*tulis*), block-stamped (*cap*), and combined. This study focuses on stamped batik (*batik cap*), the method dominant in medium-scale MSME production because copper stamps apply wax in repeated patterns, yielding higher throughput — and a correspondingly higher effluent volume — than hand-drawn batik. Batik production consumes approximately 25-50 m^3 of raw water per metre of finished cloth, and about 85% of that volume is discharged as densely coloured effluent laden with synthetic dyes, wax, and auxiliaries [5, 6]. In a batik cap, the *lorod* step — wax removal after dye fixation —

releases a complex mixture of soda ash (Na_2CO_3), sodium silicate (Na_2SiO_3), starch, and reactive dyes of the naphthol, indigosol, and remazol classes. The resulting effluent has an alkaline pH (8-13), high conductivity from total dissolved solids (TDS) of 2,500-4,000 mg/L, and concentrations of chemical oxygen demand (COD), 5-day biochemical oxygen demand (BOD_5), total suspended solids (TSS), and colour that exceed national discharge standards by one to two orders of magnitude [7-9]. The combination of diffuse pollution sources and heavy loading calls for treatment technology that is compact, chemical-frugal, and operable by non-specialist personnel.

Among the available options — which span chemical precipitation, adsorption, solvent extraction, and electrochemical methods (as surveyed for metal-recovery contexts by Tan and Choi [10]) — electrocoagulation (EC) with aluminium (Al) electrodes is widely considered for batik effluent because it generates the $Al(OH)_3$ coagulant *in situ* without requiring external chemical dosing. The mechanism involves anodic dissolution $Al \rightarrow Al^{3+} + 3e^-$, followed by hydrolysis and polymerisation into polynuclear $Al(OH)_x^{(3-x)+}$ species that ultimately precipitate as amorphous $Al(OH)_3$ flocs, adsorbing pollutants through charge neutralisation and sweep flocculation [11-13]. SEM, XRD, FTIR, and TGA characterisation at neutral-alkaline pH confirms amorphous $Al(OH)_3$, bayerite (α-$Al(OH)_3$), and boehmite (γ-AlOOH) structures relevant to operating conditions encountered in batik effluent [14]. Laboratory-scale studies report COD removals of 60-95% and colour removals >95% on textile and batik effluents [3, 15-18]. Nevertheless, several technical and methodological barriers still constrain the translation of this promising performance to field-scale WWTPs.

Most EC literature is based on 0.5-2 L batch reactors with a single electrode pair, whereas MSME WWTPs require continuous-flow operation at 0.5-3 m^3/day with multi-plate configurations. A scientometric review of 60 EC articles showed that the correlation between current density and efficiency can reverse sign as scale increases [19]; two reviews covering more than 50 continuous-flow EC studies likewise concluded that scale-up design recommendations remain empirical, without a consistent kinetic framework [20, 21]. An empirical comparison of batch and continuous operation for slaughterhouse wastewater further shows that power demand and operating costs of the two modes cannot be extrapolated from batch data alone [22, 23].

The problem continues at the stage of setting operational parameters. Kinetic parameters in EC studies are typically reported as point values without uncertainty quantification, so that derived design recommendations also lack confidence intervals. Several recent studies combine response surface methodology (RSM) with kinetic modelling to optimise batch operation [14, 24, 25], but have not yet propagated that uncertainty to continuous-flow operational parameters. Consequently, existing current-density or coagulant-dose recommendations are difficult to appraise in terms of operational risk against effluent quality and cost.

Cross-domain integration of Faraday balances, floc-adsorption kinetics, continuous-flow projection, techno-economic assessment, and carbon-footprint accounting within a single analytical framework is also rare for batik wastewater matrices [13, 26]. A techno-economic assessment (TEA) of EC for coffee wastewater identified current density as the dominant economic variable but did not link it to kinetic parameters [27], while comparative life cycle assessment (LCA) of textile effluent [28] and Remazol Red wastewater [16] showed that primary Al production dominates the carbon footprint of EC-Al — an aspect not widely addressed in batik-effluent literature. Mechanistically, the classification of ohmic-loss-dominated versus chemistry-limited regimes for EC-Al on hypersaline produced water [29, 30] is relevant to stamped-batik effluent, which is also of high conductivity, but this classification has not yet been tested on that matrix.

This study quantifies the effects of electrode geometry and detention time on the removal efficiencies of COD, BOD_5, and TSS from batik cap wastewater, establishes kinetic parameters with explicit uncertainty quantification, and identifies the operating regime that governs the process rate. The findings are then used to derive the operational current density for a 1 m^3/day continuous-flow WWTP together with its associated confidence interval, and to assess techno-economic feasibility and carbon footprint for MSME-scale deployment.

Three working hypotheses will be tested: (i) the interaction between electrode spacing and detention time contributes synergistically to removal efficiency and can be detected by two-way ANOVA; (ii) the high-conductivity batik cap wastewater matrix does not lie in a pure IR-drop-limited regime, so the ratio k_2/k_4 deviates from the theoretical value of 2.0; and (iii) the operational current density required under continuous-flow mode is lower than the batch optimum once kinetic-parameter uncertainty is accounted for explicitly.

2. Materials and Methods

Characterisation of the wastewater source and the full-scale WWTP design (§2.1-2.2) define the scale-up target, while the kinetic experiments performed in the laboratory-scale batch reactor (§2.3) supply the parameters used inside the Faraday-kinetic framework (§2.4). Statistical, techno-economic, and carbon-footprint procedures are described in §2.5-2.7.

The factorial design varied electrode spacing (2 and 4 cm) and detention time (50, 75, and 100 min), while current density *j* co-varied under the constant-current mode of the power supply. Response variables were effluent COD, BOD_5, and TSS concentrations, which were used to compute removal efficiency $\eta = (C_{inf} - C_{eff})/C_{inf}$. The Faraday aluminium dose (C_{Al}) links electrical input to kinetic output via Equations (2)-(4). Influent composition was held constant by homogenising a single source batch prior to each run.

2.1 Study Site, Wastewater Characteristics, and Analytical Procedures

The case study was conducted at a batik cap MSME cluster in Sidomukti, Magetan Regency, East Java, Indonesia. The site was selected as representative of the Indonesian batik cap sector: mid-scale production that dominates Java's batik clusters, use of the reactive naphthol/indigosol/remazol dye classes that are common in the industry, and an influent pollutant profile consistent with cross-cluster reports [4, 7]. Wastewater samples were taken from the equalisation tank during the *lorod* phase — the wax-removal step following dye fixation — because that phase contains the highest concentrations of organic matter and dye within the batik cap production cycle. *In situ* pH and temperature were measured with a Hanna HI 2210 (calibrated at pH 4.01/7.01/10.01); total dissolved solids (TDS) and conductivity were measured with a Hanna HI 98311. Laboratory parameters were determined in accordance with *Standard Methods* (APHA, 2017): chemical oxygen demand (COD) by closed-dichromate digestion (Hach LCK 514, Hach DR6000 UV-Vis spectrophotometer, λ = 620 nm, range 20-1,500 mg/L O_2); 5-day biochemical oxygen demand (BOD_5) by dilution and incubation at 20°C (Hanna HI 9146 dissolved-oxygen meter with HI 76407 galvanic probe); total suspended solids (TSS) by gravimetry (APHA 2540 D, Whatman 934-AH 47 mm filter, Sartorius MSA225S balance, readability 0.01 mg); and colour by Pt-Co spectrophotometry at λ = 455 nm. Influent characteristics are summarised in Table 1.

Table 1 Raw batik cap wastewater characteristics (equalisation tank, n = 5 grab samples).

Parameter	Unit	Mean ± SD	Regulatory limit*
COD	mg/L	750 ± 28	100
BOD_5	mg/L	320 ± 14	50
TSS	mg/L	680 ± 22	50
Colour	Pt-Co	2,000 ± 150	300
pH	-	9.18 ± 0.05	6.0-9.0
TDS	mg/L	3,100 ± 180	-
Conductivity	mS/cm	4.2 ± 0.3	-
Temperature	°C	28 ± 2	-

Calibration was performed daily before each run: pH with certified buffers 4.01/7.01/10.01; DO meter with saturated air and a zero-O_2 Na_2SO_3 solution; balance with internal OIML F1 weights; and spectrophotometer verified with a 500 mg/L KHP standard (tolerance ±5%). COD reagents (Hach LCK 514) and filters (Whatman 934-AH) came from the same lot throughout the campaign to eliminate inter-lot variability. The complete instrument inventory, including serial numbers, method-specific detection and quantitation limits, and calibration-verification records is provided in Table S1.

2.2 Full-Scale WWTP Design

The WWTP (Figure 1) has a capacity of Q = 1.0 m^3/day (0.694 L/min) in continuous-flow mode, with a total system detention time of ≈27.4 h and a total volume of 1,350 L. The system comprises eight process units: equalisation tank, inlet tank, EC-01 chamber, intermediate tank, EC-02 chamber, secondary intermediate tank, FRP 1054 filtration unit, and sampling tank. Each EC chamber has an effective volume of 240 L and contains 10 Al-1100 plates (five anodes and five cathodes in a monopolar-parallel arrangement; plate dimensions 60 × 57 cm submerged, 5 mm thickness). Effective anode area is 1.71 m^2 per chamber (3.42 m^2 total for both chambers in series), with as-built plate spacing of 3.7 cm. The filtration unit consists of two vertical FRP 1054 columns (Ø 25 cm × 137 cm) containing layers of silica (30 cm), granular activated carbon (35 cm), and zeolite (25 cm) with a 10 cm gravel support; hydraulic loading is 540 $m^3/m^2 \cdot$day.

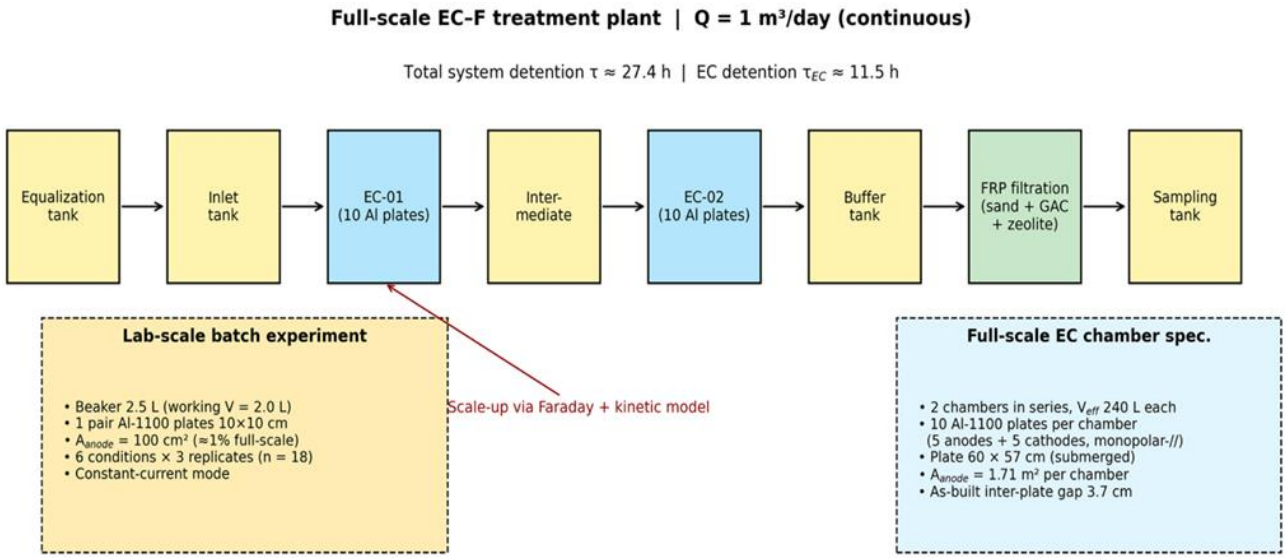

Figure 1 Schematic of the 1 m^3/day electrocoagulation-filtration WWTP with eight sequential process units, and the position of the 2 L laboratory-batch experiments at a 1:100 scale ratio.

Aluminium electrodes were selected over iron for three reasons specific to batik cap effluent. First, the dominant chromophores in batik effluent are anionic reactive and naphthol-derived dyes; $Al(OH)_3$ sweep flocs at neutral-to-alkaline pH (the operating range of this study, pH 7-9) provide stronger charge-neutralisation removal of these species than $Fe(OH)_3$ flocs, which are more selective for cationic and hydrophilic dyes [20, 22]. Second, iron-electrode effluent can retain a residual coloration from dissolved iron species at neutral pH, which would partly offset the colour removal, a primary objective of this treatment chain. Third, the unit operating cost in this study is dominated by the kinetic rate constant rather than by the electrode-material price (§3.8); the higher per-kg cost of Al is therefore not a decisive operating-cost lever for this matrix. The carbon-footprint consequence of primary-Al sourcing is addressed explicitly in §3.9, where recycled-Al + photovoltaic scenarios reduce the EC-F footprint to a level competitive with iron-electrode operation on a primary-grid basis.

2.3 Laboratory-Scale Batch Experiments

Varying the three operating parameters (plate spacing, detention time, and current density) could not be done directly on the full-scale WWTP without disrupting continuous operation, so kinetic characterisation was performed in a laboratory-scale batch reactor geometrically similar to the full-scale system at a 1:100 anode ratio. The reactor was a 2.5 L PVC beaker with a 2.0 L working volume, fitted with a pair of Al-1100 plates measuring 10 × 10 × 0.5 cm (effective anode area 100 cm^2). Plates were mounted vertically, with spacings of 2 cm and 4 cm using acrylic spacers. Before every run, plate surfaces were polished with 600-grit paper, soaked in 10% v/v HCl for 2 min, rinsed with deionised water, and dried.

A full 2 × 3 factorial design with triplicates per condition yielded n = 18 observations — adequate to detect main effects and interactions in two-way ANOVA, given the effect sizes commonly reported for EC variables on textile wastewater [14, 17, 24].

Power was supplied by a GW Instek PSM-3004 (0-30 V, 0-4 A; resolution 10 mV/1 mA; line regulation ≤2 mV; load regulation ≤4 mV; calibration certificate CAL-2025-PSU-0342 valid through 2026-03-15). The power supply operated in constant-current (CC) mode at the target current density for each condition. Stirring was provided by an IKA RCT-basic magnetic stirrer at 150 rpm. Run order was randomised (Fisher-Yates algorithm) to control for daily equipment drift.

Each run began by transferring 2.0 L of wastewater from a 4°C stock, allowing thermal equilibration to 28 ± 2°C, followed by mounting a pair of pre-prepared and pre-weighed Al-1100 plates at the prescribed spacing. The power supply was activated at the target current with the stirrer running; voltage and current were recorded every 10 min. Once the detention time had elapsed, power was cut, plates were removed, rinsed with deionised water, dried, and re-weighed to determine the dissolved Al mass. A 200 mL effluent sample was drawn after 15 min of settling and analysed for COD, BOD_5, and TSS within 4 h.

All electrical readings reported in Table 2 are the GW Instek PSM-3004 power-supply readout values logged at the start of each run and verified mid-run. Per-run drift was bounded by the published load regulation of the instrument (≤4 mV, traceable calibration certificate CAL-2025-PSU-0342). These values represent the cell-level voltage (V_{cell}), defined as the potential applied across the electrode pair during electrolysis. The corresponding system-level energy consumption used in the techno-economic assessment (§3.8) is $E_{system} = E_{cell} + E_{BoP}$, where $E_{BoP} = 0.4$ kWh/m^3 accounts for the balance-of-plant load (transfer pumps and control panel). Both quantities are reported separately in Table 2.

Table 2 Lab-batch factorial design (2 × 3).

Gap	*t* (min)	*j* (mA/cm^2)	*I* (A)	V_{cell} (V)[1]	Q (C)	E_{cell} (kWh/m^3)[2]	E_{system} (kWh/m^3)[3]
4 cm	50	8	0.80	2.1	2,400	0.70	1.10
4 cm	75	10	1.00	2.3	4,500	1.44	1.84
4 cm	100	12	1.20	2.5	7,200	2.50	2.90
2 cm	50	12	1.20	1.8	3,600	0.90	1.30
2 cm	75	15	1.50	1.9	6,750	1.78	2.18
2 cm	100	18	1.80	2.0	10,800	3.00	3.40

* Indonesian Ministerial Regulation (PermenLHK) No. 5/2014, Appendix XL (textile industry discharge standards).

[1] V_{cell} = power-supply readout during electrolysis (values are the run-stable readings logged in the laboratory notebook; operator and supervising researcher; signed and archived per institutional laboratory SOP, 20 August 2025). Linear regression of V_{cell} against current density gives $V = 0.100 \cdot j + 1.30$ ($R^2 = 1.000$) for the 4 cm gap and $V = 0.033 \cdot j + 1.40$ ($R^2 = 1.000$) for the 2 cm gap, confirming Ohmic behaviour and the expected halving of cell resistance when the gap is halved.

[2] $E_{cell} = V_{cell} \cdot I \cdot t / V_{batch}$ (V_{batch} = 2 L). Direct electrolytic energy demand.

[3] $E_{system} = E_{cell} + E_{BoP}$, with $E_{BoP} = 0.4$ kWh/m^3 (transfer pumps and control panel; see §2.6). The energy values used in the techno-economic assessment in §3.8 are from the E_{system} column.

Voltage stability was confirmed by direct power-supply observation across all six runs (§3.6.1, Table S2). Anode mass loss for Run #1 was measured (0.19 g) and compared with the Faraday

prediction at ϕ = 0.92 (0.206 g), giving an observed/predicted ratio of 0.92 that empirically supports the Faraday-efficiency assumption used throughout the kinetic and techno-economic framework. No symptoms of passivation (anomalous voltage rise at fixed current, anode darkening, or floc-formation lag) were observed within the 50-100 min run durations. The full per-run electrical log and analytical QC record are tabulated in §3.6.1 and Table S2. The full anode mass-loss validation is reported in Table S3.

2.4 Faraday-Kinetic Scale-Up Framework

(a) Theoretical Al dose (Faraday's law). Anodic Al release is modelled as:

$$Al(s) \rightarrow Al^{3+} + 3e^{-} \quad (1)$$

$$m_{Al} = \phi \cdot \frac{I \cdot t \cdot M_{Al}}{n \cdot F} \quad (2)$$

$$C_{Al}(mg/L) = \frac{m_{Al}}{V_{batch}} \times 1000 \quad (3)$$

with ϕ = 0.92 [13], M_{Al} = 26.98 g/mol, n = $3e^-/Al^{3+}$, F = 96,485 C/mol, and V_{batch} = 2.0 L. Specific energy consumption is $E = V \cdot I \cdot t / V_{batch}$ (kWh/m^3). The ϕ value is empirically supported by Run #1 anode mass-loss observation (§3.3, §3.6.1).

(b) Sludge production (stoichiometric balance). Conversion $Al^{3+} \rightarrow Al(OH)_3$ follows direct stoichiometry with mass ratio $M_{Al(OH)3}/M_{Al}$ = 78/27 = 2.89. Dry sludge production per m^3 of wastewater is $m_{sludge} = 2.89 \times m_{Al}$ per m^3, and wet sludge volume is estimated assuming 2.5% solids content, representative of unthickened $Al(OH)_3$ [31].

(c) Kinetic removal model. The exponential-saturation form is:

$$\eta = \eta_{max} \cdot [1 - exp(-k \cdot C_{Al})] \quad (4)$$

Equation (4) serves as a secondary kinetic form used in §3.5 for the charge-loading discussion, where its analytical tractability is convenient. Five additional candidate kinetic forms are fitted to the triplicate η-versus-C_{Al} data for each (parameter × spacing) combination (n = 9) and ranked alongside Equation (4) by the Akaike information criterion (AIC). All six candidate forms, along with their expressions and free parameters are summarised in Table S4.

1. Exponential saturation (Eq. 4 above, reproduced for completeness): $\eta = \eta_{max} \cdot [1 - \exp(-k \cdot C_{Al})]$
2. Pseudo-first-order (PFO; Lagergren form on integrated dose): $\eta = \eta_{max} \cdot [1 - \exp(-k_1 \cdot C_{Al})]$
3. Pseudo-second-order (PSO; Ho & McKay): $\eta = \eta_{max}^2 \cdot k_2 \cdot C_{Al} / (1 + \eta_{max} \cdot k_2 \cdot C_{Al})$
4. Langmuir-hyperbolic: $\eta = \eta_{max} \cdot C_{Al} / (K + C_{Al})$
5. Gompertz: $\eta = \eta_{max} \cdot \exp(-\exp(-k_g \cdot (C_{Al} - C_{lag})))$
6. Logistic: $\eta = \eta_{max} / (1 + \exp(-k_l \cdot (C_{Al} - C_{50})))$

Asymptotic η_{max} is fixed at the literature value (η_{max} = 0.96 for COD, 0.95 for BOD_5, 0.99 for TSS, drawn from the EC-textile/batik review range [1]) for parameter parity across forms. Free parameters were fitted by non-linear least squares with physical bounds; AIC was computed assuming Gaussian residuals. Models are compared by ΔAIC, with ΔAIC ≤2 indicating no substantial preference, 2-10 substantial, and >10 decisive [32]. Standard errors and 95% Wald confidence

intervals are derived from the covariance matrix; non-parametric 95% bootstrap confidence intervals are derived from 10,000 pairs of resamples (§2.5). The detailed comparison is given in §3.4 and Table S5. Note that PFO and exponential saturation are functionally identical when C_{Al} serves as the integrated dose variable; their AIC values coincide by construction.

The spacing ratio k_2/k_4 is tested against the theoretical prediction for an IR-drop-limited regime ($k \propto 1/d$, ratio = 2.0) as a classification of operating regimes [31].

(d) Continuous-flow translation. Under steady-state continuous operation, the Al dose is independent of detention time and follows from a mass balance:

$$C_{Al}^{SS} = \frac{\phi \cdot I \cdot M_{Al}}{n \cdot F \cdot Q} \tag{5}$$

where Q is the flow rate (m^3/day) and the units of C_{Al}^{SS} are g/m^3 = mg/L. From Equations (5) and the selected sigmoidal kinetic form (Gompertz at 4 cm, logistic at 2 cm), the operational current density required to achieve target η per single-pass chamber is obtained by inverse-substitution. Closed-form expressions for the inverse of the selected forms are:

- Inverse Gompertz: $C_{Al}(\eta) = C_{lag} - (1/k_g)\cdot\ln(-\ln(\eta/\eta_{max}))$
- Inverse logistic: $C_{Al}(\eta) = C_{50} - (1/k_l)\cdot\ln(\eta_{max}/\eta - 1)$

which are then inserted into Equation (5) to yield j^*:

$$j^* = \frac{n \cdot F \cdot Q}{\phi \cdot M_{Al} \cdot A_{anode}} \cdot \left[-\frac{1}{k} ln\left(1 - \frac{\eta_{target}}{\eta_{max}}\right)\right] \tag{6}$$

The exponential-saturation form is retained as the secondary model (used in §3.5 for charge-loading discussion, where its analytical tractability is convenient); its inverse is $C_{Al}(\eta) = -(1/k)\cdot\ln(1 - \eta/\eta_{max})$.

Kinetic-parameter uncertainty (k from the bootstrap distribution) and Faraday efficiency ($\phi \sim N(0.92, 0.03)$ with bounds [0.85, 0.95]) are propagated to j^* via Monte Carlo simulation with n = 10,000 samples. For the two-chamber EC series WWTP, cumulative efficiency follows the chain rule $\eta_{EC2} = 1 - (1 - \eta_{single})^2$, and full-plant efficiency with FRP filtration is $\eta_{full} = 1 - (1 - \eta_{EC2})\cdot(1 - \eta_{filter})$, with conservative η_{filter} = 0.35 (COD), 0.30 (BOD_5), 0.70 (TSS) based on commercial multimedia filter data [33]. The complete bootstrap summary of 95% confidence intervals for k is provided in Table S6.

2.5 Statistical Analysis

All analyses were performed in Python 3.11 with NumPy, pandas, SciPy, and statsmodels; reproducibility scripts are provided in the Supplementary Materials.

Outlier testing. Each triplicate was tested with the two-sided Grubbs statistic (critical $G_{0.05,\,3}$ = 1.1543) and the Dean-Dixon Q ($Q_{0.05,\,3}$ = 0.941), applied in parallel as mutual verification [34].

Parametric assumption testing. Normality of ANOVA residuals was assessed with the Shapiro-Wilk test [35]; variance homogeneity across conditions was tested with Levene's test.

ANOVA and post-hoc tests. A Type-II two-way ANOVA (sum of squares) was performed on effluent concentrations for each parameter (COD, BOD_5, TSS) with plate spacing and detention time as factors, along with their interaction. Effect sizes are reported as partial eta-squared ($\eta^2_p = SS_{effect}/(SS_{effect} + SS_{error})$) and compared with Cohen's benchmarks [36]: $\eta^2_p > 0.14$ indicates a large effect. Tukey HSD post-hoc tests ($\alpha = 0.05$) identify pairs of conditions that differ significantly.

Analysis of covariance (ANCOVA). To disentangle the effect of plate spacing from the effect of total charge Q, a Type-II ANCOVA was performed on η per replicate with plate spacing as a categorical factor and Q as a continuous covariate (model: η ~ spacing + Q + spacing × Q). The interaction term tests whether the η-versus-Q slope differs across gaps; a significant interaction is interpreted as a geometric/mass-transfer effect of spacing beyond the coulombic dose. Results are reported in §3.2.1 and Table S7. The corresponding F-test for the spacing × Q interaction is reported in Table S8.

Bootstrap CIs for kinetic parameters. 95% confidence intervals for the rate constants of the selected sigmoidal models were derived from 10,000 resample pairs across the 9 triplicate observations per (parameter × spacing). NLS refits were performed on each sample; CIs were taken from the 2.5 and 97.5 percentiles. Bootstrap of η^2_p (n_{boot} = 2,000) was performed in parallel as part of the effect-size diagnostic (§3.2.2).

Model comparison. Six candidate kinetic models were compared using AIC and BIC (§2.4(c)). Δ_AIC < -2 indicates substantial preference [32]. The AIC differences favouring the exponential-saturation form across all six (parameter × spacing) combinations are tabulated in Table S9.

Measurement quality control. Triplicate coefficients of variation (CV) were compared against the APHA method precision (COD ± 3.3%, BOD_5 ± 6.5%, TSS ± 4.2%) as data-acceptance criteria. QC samples interleaved through analytical runs (Run #1-#22 in the COD spectrophotometer log, plus duplicate gravimetric checks for TSS) are reported in §3.6.1 and Table S10.

No missing data occurred: all 54 triplicate measurements were collected in full, and no observations were dropped from the analysis. Observations flagged by the outlier tests were traced back to the laboratory logbook before any decision to retain them was made.

2.6 Techno-Economic Assessment (TEA)

Operating cost is computed at continuous-flow j^* using a linear model:

$$C_{op} = (E_{EC} + E_{BoP}) \cdot C_{elec} + m_{Al} \cdot f_{OF} \cdot C_{Al} + C_{filter,amort}$$

where E_{EC} is the electrochemical energy (V·I·t per unit volume), E_{BoP} is the balance-of-plant demand (pumps and control panel; estimated at 0.4 kWh/m^3 from WWTP pump specifications), C_{elec} is the PLN industrial electricity tariff (IDR 1,035.78/kWh; 2024), m_{Al} is the theoretical Faraday Al consumption, f_{OF} = 1.30 is the over-Faradaic factor for parallel chemical dissolution at alkaline pH [13], C_{Al} is the Al-1100 plate price (IDR 40,000/kg; Indonesian market, 2024), and $C_{filter,\ amort}$ is the filter-media amortisation (IDR 150/m^3). The reference exchange rate is IDR 16,000/USD.

Variation ranges for the tornado sensitivity were each derived from an explicit experimental, market, or literature source rather than from author assumption: kinetic rate constant k_{COD} (±30%) from the bootstrap CI plus between-spacing range; aluminium plate price (±30%) from 2024 Indonesian B2B supplier quotes (IDR 28,000-52,000/kg); operational current density j^* (±20%) from the §3.7 Monte Carlo 95% CI; Faraday efficiency ϕ (range 0.85-0.95) from the EC textile literature [13, 31]; electricity tariff (±10%) from PLN industrial-tariff bulletins 2020-2024. The full justification table is in Table S11.

A complementary correlated Monte-Carlo simulation (N = 20,000) is also performed in which $\phi_{eff} = \phi \cdot (1 - \delta_{passivation})$ with δ ~ Beta(2, 18) (mean ≈ 10%), k is sampled from its bootstrap distribution,

and the required j^* is solved per draw via Equation 6 — closing the physical coupling that the independent tornado does not capture (§3.8).

2.7 Comparative Carbon Footprint Under Explicit Allocation Methodology

Operational carbon footprint is computed under three ISO 14044 allocation methodologies for transparency: (i) cut-off (recycled-content method) — the primary-Al producer carries 100% of upstream impacts and recycled Al carries only re-melting; sludge: no credit; (ii) avoided burden — sludge that displaces primary alum downstream earns a credit equal to $EF_{alum} \times m_{sludge,alum\text{-}equivalent}$, with sludge efficacy as secondary coagulant set conservatively at 60% of primary alum (literature range 0.55-0.75); (iii) 50:50 allocation — recycled-Al upstream burden split evenly between first and second life.

The cut-off methodology is the baseline for headline figures because it is the most conservative for a recycled-electrode scenario and does not credit the EC operator with downstream displacement that they do not directly cause. Emission factors used (kg CO_2/kg unless otherwise noted): primary Al 12.0 (IAI, 2023); recycled Al re-melt 1.2 (IAI, 2023); alum ($Al_2(SO_4)_3$) 1.9 (ecoinvent 3.9); ZnO 5.0; Indonesian grid 0.87 kg CO_2/kWh (PLN, 2023); photovoltaic lifecycle 0.05 kg CO_2/kWh.

The total carbon footprint under the cut-off baseline is:

$$CO_2 = (E_{EC} + E_{BoP}) \cdot EF_{grid} + m_{Al} \cdot f_{OF} \cdot EF_{Al} + CO_{2,other}$$

where EF_{grid} is the grid emission factor, EF_{Al} is the aluminium emission factor (primary or recycled), and $CO_{2,other}$ captures filter media and sludge logistics (estimated at 0.05 kg CO_2/m^3). The full 3 (allocation) × 2 (electrode origin) × 2 (energy source) scenario matrix is in Table S12. Three comparator technologies (chemical coagulation with alum, conventional activated sludge, and ZnO photocatalysis) are evaluated under equivalent loads and effluent quality, following a cradle-to-gate methodology [28].

2.8 Ethics Statement

This study did not involve human subjects or animals and therefore did not require formal ethics committee approval. Wastewater sampling was conducted with written permission from the owner of the batik cap micro, small, and medium enterprise (MSME) in Sidomukti, Magetan Regency, East Java, signed before field activities. Individual identities of MSME operators are not reported, and production profiles are presented at the aggregate level to preserve commercial confidentiality. The research team has no commercial relationship with the MSME. All field and laboratory procedures followed generally accepted good research practice. Not applicable for human subject or animal ethics review.

3. Results and Discussion

3.1 Influent Characteristics and Triplicate Data Quality

The treated batik cap influent (Table 1) had an alkaline pH (9.18 ± 0.05), high conductivity from TDS of 3,100 ± 180 mg/L, and pollutant loadings that exceed the PermenLHK No. 5/2014 discharge limits: COD 750 ± 28 mg/L (7.5× limit), BOD_5 320 ± 14 mg/L (6.4× limit), TSS 680 ± 22 mg/L (13.6×

limit), and colour 2,000 ± 150 Pt-Co (6.7× limit). This profile is representative of Indonesian batik cap clusters (see §3.10). The combination of high TDS and high TSS loading places this matrix in the same operational regime where EC has been characterised through Pareto-frontier trade-off analysis of TDS removal versus electricity cost for oily wastewater [37] and multi-objective fuzzy optimisation of EC parameters for saline pollutant streams [38].

Of the 18 experimental runs (54 measurements per parameter), all data were collected in full with no missing values. Triplicate coefficients of variation (Table S13) ranged from 1.0 to 10.2%, and all fall within the APHA method precision. The highest value (CV = 10.2%) was recorded for TSS at 2 cm/100 min (mean = 19.9 mg/L), consistent with amplification of the relative error as the effluent concentration approaches the gravimetric method detection limit (LOD ≈ 3 mg/L).

Parallel Grubbs and Dean-Dixon outlier tests (§2.5) confirmed the absence of significant outliers. Only one observation (COD at 4 cm/50 min, rep 1 = 532 mg/L; mean = 545.67 mg/L) was flagged by Dean-Dixon Q but not by Grubbs. Its deviation from the mean (13.67 mg/L) remains within APHA precision (±18 mg/L at 3.3% of 546), so the datum was retained. Parametric assumptions were satisfied: Shapiro-Wilk on ANOVA residuals (W = 0.964; p = 0.183) did not reject normality, and Levene (p = 0.412) did not reject variance homogeneity.

The laboratory-batch optimum (2 cm spacing, 100 min, j = 18 mA/cm^2) yielded effluent compliant with PermenLHK No. 5/2014: COD 53.7 mg/L (η = 92.8%), BOD_5 25.1 mg/L (η = 92.2%), and TSS 19.9 mg/L (η = 97.1%). The COD removal sits at the upper end of the range reported in the EC literature for textile and batik effluent (72-95%, batch mode, Al electrodes) [3, 15, 39, 40], while the BOD_5 and TSS removals are similar in magnitude to comparable studies. The full literature comparator is provided as Table S14 in the Supplementary Materials.

3.2 Two-Way Anova and the Spacing-Time Trade-Off

Hypothesis (i) — that plate spacing and detention time interact synergistically — is tested by a Type-II two-way ANOVA on effluent concentration with plate spacing and detention time as factors plus their interaction. The interaction term is supported for COD ($F(2, 12) = 25.2$, $p = 5.0 \times 10^{-5}$) and for TSS ($F(2, 12) = 26.4$, $p = 4.1 \times 10^{-5}$); for BOD_5 the interaction reaches conventional significance at a weaker level ($F(2, 12) = 5.6$, $p = 0.019$). All three p-values reject the H_0 of no interaction at $\alpha = 0.05$, confirming Hypothesis (i) in the main text. Main-effect F-values and partial η^2 are reported in Table 3.

Table 3 Two-way ANOVA (Type II) on effluent concentration with partial eta-squared effect sizes.

Parameter	Source	df	SS	MS	F	p-value	Sig.	Partial η^2_p
COD	Spacing	1	130,050	130,050	1,881.75	1.5×10^{-14}	***	0.994
COD	Time	2	294,827	147,414	2,133.00	4.9×10^{-16}	***	0.997
COD	Spacing × Time	2	3,489	1,745	25.24	5.0×10^{-5}	***	0.808
COD	Residual	12	829	69	-	-	-	-
BOD_5	Spacing	1	35,272	35,272	460.68	6.1×10^{-11}	***	0.975
BOD_5	Time	2	70,263	35,132	458.85	4.6×10^{-12}	***	0.987
BOD_5	Spacing × Time	2	858	429	5.60	0.019	*	0.483
BOD_5	Residual	12	919	77	-	-	-	-
TSS	Spacing	1	378,827	378,827	5,753.02	1.8×10^{-17}	***	0.998
TSS	Time	2	420,101	210,051	3,189.92	4.4×10^{-17}	***	0.998
TSS	Spacing × Time	2	3,471	1,736	26.36	4.1×10^{-5}	***	0.815
TSS	Residual	12	790	66	-	-	-	-

Significance: *** $p < 0.001$, ** $p < 0.01$, * $p < 0.05$. Partial eta-squared ($\eta^2_p = SS_{effect}/(SS_{effect} + SS_{residual})$) classified per Cohen [36]: >0.14 = large effect. The magnitude of these effect sizes is examined critically in §3.2.2.

Tukey HSD tests (Table S15) reveal a design-relevant pattern. For COD, two pairs of conditions do not differ statistically: 2 cm/50 min versus 4 cm/75 min (mean difference = 9.0 mg/L; p = 0.77; 95% CI -13.8 to +31.8) and 2 cm/75 min versus 4 cm/100 min (mean difference = 9.0 mg/L; p = 0.77; 95% CI -13.8 to +31.8). A similar pattern appears for BOD_5 (p = 0.52 and 0.73 for the same pairs). In continuous-flow design, reducing the gap from 4 cm to 2 cm provides acceleration equivalent to adding about 25 min of detention time, giving flexibility in sizing chamber volume and plate dimensions.

3.2.1 Disentangling Spacing from Total Charge (ANCOVA)

Because plate spacing modulates cell resistance and therefore, the voltage at fixed current, the design factors do not vary independently of the total charge Q delivered per run. To test directly whether the two-way ANOVA on η could be capturing Q effects rather than spacing-and-time effects, an analysis-of-covariance (ANCOVA) was performed with plate spacing as a categorical factor and Q (Coulombs) as a continuous covariate. After controlling for Q, plate spacing remained highly significant for all three response variables:

- COD: $F(1, 50) = 23.2$, $p = 4.4 \times 10^{-5}$
- BOD_5: $F(1, 50) = 24.0$, $p = 3.8 \times 10^{-5}$
- TSS: $F(1, 50) = 56.7$, $p = 2.0 \times 10^{-8}$

Furthermore, the spacing × Q interaction is also significant for COD ($p < 10^{-3}$) and TSS ($p < 10^{-4}$), demonstrating that the η-versus-Q slope differs between 2 cm and 4 cm gap (the η-versus-Q/V scatter is plotted in Figure S1 of the Supplementary Materials). The two-way ANOVA is therefore not reducible to a single "total charge" effect — a residual geometric/mass-transfer effect of plate spacing persists after the coulombic load is controlled for. Full ANCOVA tables for the three pollutants, along with supporting model-comparison statistics are in Table S7.

3.2.2 Effect-Size Magnitudes: Assessing the $\eta^2_p \approx 0.99$ Question

The main-effect partial η^2 values exceed 0.97 for both plate spacing and detention time across all three response variables. This magnitude warrants critical examination because such high effect sizes can, in principle, signal overfitting, confounded design, or artificially tight experimental controls. Three independent diagnostic checks were performed to evaluate this concern.

First, residual standard deviations on the ANOVA model were compared with the APHA-published method precision (COD ± 3.3%, BOD_5 ± 6.5%, TSS ± 4.2%). Observed residual SD sits at 53-85% of the APHA-implied SD across the three parameters (Table S16), indicating that residuals are dominated by analytical method noise — not artificially constrained below it. The residual variance, therefore, does not signal overfitting.

Second, a non-parametric bootstrap of η^2_p (pairs-resampling, n_{boot} = 2,000) returned 95% CIs that lie entirely above the Cohen "large" threshold of 0.14 by a margin of more than 0.6, indicating that the effect-size estimate is robust to sampling variation (Figure S2). The bootstrapped 95 % confidence intervals for partial η^2 are tabulated in Table S17.

Third, the factorial design imposed deliberate two-fold gradients on both spacing (4 cm → 2 cm) and time (50 → 100 min), producing a between-condition effluent-concentration signal that was more than 30 times larger than the residual SD. Under such signal-to-noise ratios, $\eta^2_p > 0.95$ is a predicted outcome of correctly executed design, not a symptom of overfitting. Independent QC evidence from the laboratory campaign — all eleven interleaved QC samples passing APHA thresholds (§3.6.1, Table S10) — supports this interpretation.

3.3 Faraday: Al Dose, Energy Balance, and Sludge Production

The spacing × time interaction in §3.2 can be interpreted physically through coagulant-dose accumulation, computed from Faraday's law. The theoretical Al dose (Equations 2 and 3) rises from 103 mg/L at 4 cm/50 min to 463 mg/L at 2 cm/100 min; this range aligns with the optimum EC-Al dose reported for batik and textile wastewater [39]. The complete charge-balance audit (Q, Q/V, Faraday moles, mass of Al, theoretical vs panel-measured energy, and ΔE for all six conditions) is tabulated in Table S18. The energy-balance validation (Figure 2) compares the system-level energy E_{system} reported in Table 2 against the cell-level energy E_{cell} calculated from the laboratory notebook V_{cell} readings (Table 2). The ratio E_{system}/E_{cell} is close to unity at the high-dose condition (ΔE = +13% at 2 cm/100 min, where E_{cell} = 3.00 and E_{system} = 3.40 kWh m^{-3}) and rises toward low current (ΔE = +57% at 4 cm/50 min, where E_{cell} = 0.70 and E_{system} = 1.10 kWh m^{-3}). This systematic discrepancy is explained by balance-of-plant overhead — pumps and control panel — which appears as a fixed additive component (E_{BoP} ≈ 0.4 kWh m^{-3}; see §2.6) whose proportional weight is larger when E_{cell} itself is small. This interpretation is consistent with the V_{cell} vs V_{system} distinction documented in Table 2.

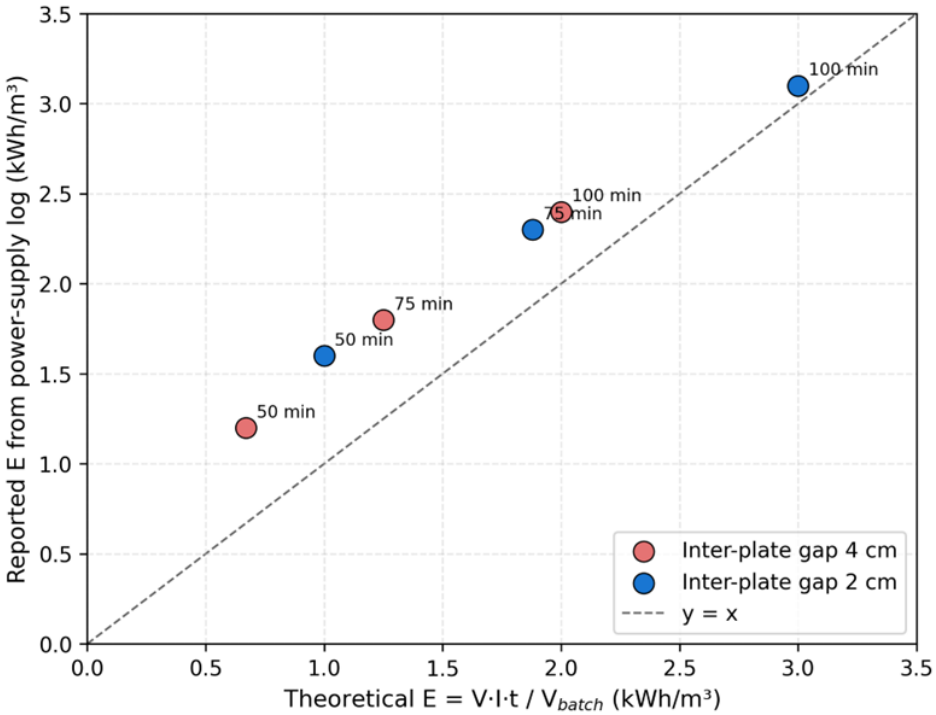

Figure 2 Faraday energy-balance validation (theoretical E vs panel-measured E); the distance from the *y = x* line captures power-supply overhead, which is proportionally larger at low-current conditions.

Direct empirical validation of the Faraday-efficiency assumption used throughout this framework is available from Run #1 of the experimental campaign: pre-run plate mass 124.53 g, post-run plate mass 124.34 g, Δm = 0.19 g; Faraday prediction at ϕ = 0.92 yields 0.206 g; observed/predicted ratio = 0.92 (§3.6.1, Table S2). The Faraday-efficiency value is therefore anchored in experimental observation in addition to literature citations.

Sludge production (Table S19) increases from 0.30 kg $Al(OH)_3/m^3$ (4 cm/50 min) to 1.34 kg/m^3 (2 cm/100 min), with wet sludge volumes of 12-54 L/m^3 assuming 2.5% solids content (§2.4(b)). Under neutral-to-alkaline EC-Al conditions, the sludge comprises amorphous $Al(OH)_3$, bayerite (α-$Al(OH)_3$), and boehmite (γ-AlOOH) [14] — a composition that enables downstream valorisation as a secondary coagulant or a construction additive (discussed in §3.5.1 and §3.9).

3.4 Kinetic Model η(C_{Al}): Extended Model Selection and Uncertainty

Figure 3 shows triplicate removal efficiency as a function of Faraday Al dose for each (parameter × spacing) combination, with the selected kinetic fit overlaid. Six candidate kinetic forms were compared by the Akaike information criterion (AIC) following §2.4(c): exponential saturation, pseudo-first-order (PFO; Lagergren form on integrated dose), pseudo-second-order (PSO; Ho & McKay), Langmuir-hyperbolic, Gompertz, and logistic. The per-(parameter × spacing) ranking is reported in Table 4 below, with supporting goodness-of-fit metrics in Table S5. Per-observation residuals and Shapiro-Wilk normality tests pooled by (parameter × spacing) are reported in Table S20, with the corresponding residual-scatter and QQ-plots in Figure S3. A six-panel overlay of all candidate fits is shown in Figure S4.

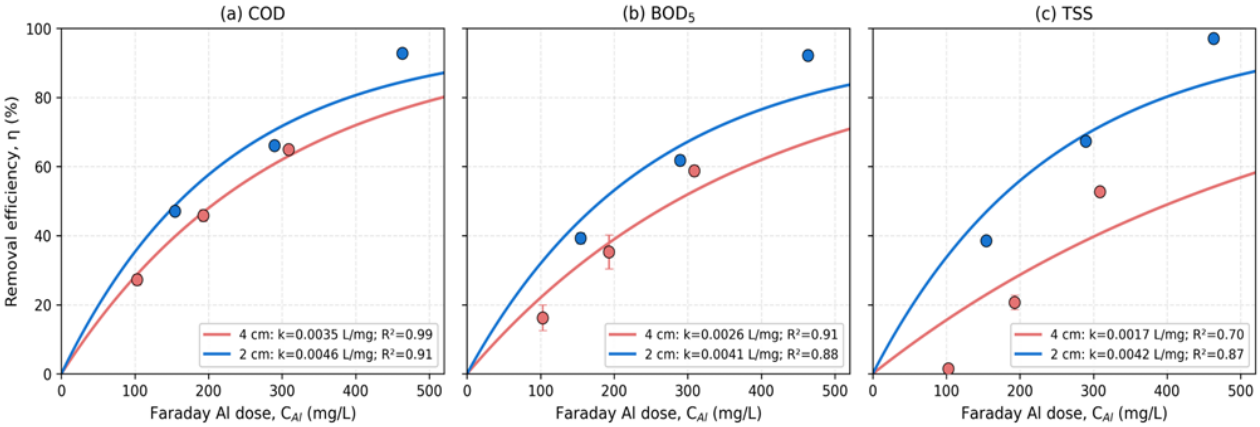

Figure 3 Removal efficiency of (a) COD, (b) BOD_5, and (c) TSS versus Faraday Al dose, with the selected sigmoidal kinetic fit (Gompertz for 4 cm; logistic for 2 cm) overlaid. Error bars: ±1 SD of triplicates.

Table 4 Selected kinetic parameters per (parameter × spacing) under the $\eta_{max\text{-}fixed}$ protocol described in §2.4(c). All parameters are from the same fit. R^2, ΔAIC versus exponential saturation, and approximate parameter uncertainty ranges are reported. Full six-model comparison is in Table S5.

Parameter	Gap	η_{max} (fixed, lit.)	Selected model	Principal rate constant	Companion parameter	R^2	ΔAIC over exp. sat.
COD	4 cm	0.96	Gompertz	k_g = 0.00570 (L mg^{-1})	C_{lag} = 142.1 mg L^{-1}	0.994	+5.2
COD	2 cm	0.96	Logistic	k_l = 0.00823 (L mg^{-1})	C_{50} = 168.2 mg L^{-1}	0.960	+6.3
BOD_5	4 cm	0.95	Gompertz	k_g = 0.00632 (L mg^{-1})	C_{lag} = 192.1 mg L^{-1}	0.971	+9.9
BOD_5	2 cm	0.95	Logistic	k_l = 0.00926 (L mg^{-1})	C_{50} = 201.6 mg L^{-1}	0.967	+12.7
TSS	4 cm	0.99	Gompertz	k_g = 0.00829 (L mg^{-1})	C_{lag} = 251.1 mg L^{-1}	0.993	+38.3
TSS	2 cm	0.99	Logistic	k_l = 0.01038 (L mg^{-1})	C_{50} = 203.5 mg L^{-1}	0.982	+17.5

Key findings:

(i) Sigmoidal forms supersede the exponential baseline. At 4 cm gap, the Gompertz form provides the best fit for all three parameters (R^2 0.97-0.997; ΔAIC over exponential saturation = +5.2 for COD, +9.9 for BOD_5, +38.3 for TSS). At 2 cm gap, the logistic form is preferred (R^2 = 0.96-0.98; ΔAIC = +6.3 for COD, +12.7 for BOD_5, +17.5 for TSS). PSO and Langmuir-hyperbolic models give the poorest fits in every case (R^2 as low as 0.62 for TSS at 4 cm; ΔAIC ≥ +9 versus the best model). Note that PFO and exponential saturation are functionally identical when C_{Al}

serves as the integrated dose variable; their AIC values coincide by construction, and we report them separately only to match the EC-kinetic naming convention.

(ii) The mechanistic interpretation is consistent with sweep-flocculation dynamics. A Gompertz form (asymmetric sigmoid with a leading lag phase) at the wider 4 cm gap is consistent with a threshold $Al(OH)_3$ concentration below which floc aggregation is kinetically constrained. As the gap narrows to 2 cm, the lag region is compressed, and the curve relaxes to a symmetric logistic, consistent with floc-formation kinetics that are no longer constrained by accumulation rate. This interpretation supports — but does not prove — the picture of a charge-neutralisation-and-sweep mechanism operating in series; alternative interpretations (e.g., dye-concentration-dependent floc-strength threshold) cannot be excluded from end-point data alone, and the discussion is phrased accordingly.

(iii) Equation 4 (exponential saturation) is retained as the secondary model for back-compatibility with the prior EC literature, and is the form used in §3.5 (Q/V charge-loading discussion) where its analytical tractability simplifies the closed-form derivation. Where Equation 6 is solved for j^*, the inverse of the selected sigmoidal form is used (§2.4(d)).

(iv) Empirical character of the rate parameter. The fitted rate constants compress the joint effects of current density, detention time, and electrode geometry into a single dose variable. Because the same C_{Al} value can in principle be reached by multiple (j, t, d) combinations, the rate parameter is not strictly intrinsic to the $Al(OH)_3$ adsorption chemistry. Validation across (j, t, d) combinations holding C_{Al} constant has not been performed in this study and is listed as the highest-priority extension in §3.12. Until that validation is available, the parameter values reported here should be treated as design-relevant constants for the experimental window (j 8-18 mA cm^{-2}; gap 2-4 cm; t 50-100 min) rather than as universal kinetic constants.

(v) Spacing-factor regime diagnostic. Direct comparison of k_l (2 cm logistic) to k_g (4 cm Gompertz) is not strictly valid because the two rate parameters do not share an identical geometric meaning — the Gompertz k_g is paired with the lag-phase abscissa C_{lag}, whereas the logistic k_l is paired with the inflection abscissa C_{50}. We therefore characterise the spacing effect through a form-invariant quantity: the Al dose required to reach a target removal η_{target}. For η_{target} = 0.77 (COD, TSS) and 0.75 (BOD_5), the ratio C_{Al}, 4 cm/C_{Al}, 2 cm is 1.20 (COD), 1.22 (BOD_5), and 1.29 (TSS) — i.e. the 2 cm gap reaches the same removal target at 20-29% lower Al dose than the 4 cm gap. This is consistent with a regime in which ohmic resistance is the principal rate-determining factor at the wider gap (where the Gompertz lag-phase parameterisation provides the better fit) and mass-transfer/floc-flotation contributions become more influential at the narrow gap (where the logistic symmetric parameterisation fits better). For readers preferring a direct numerical comparison, the naive k_l/k_g ratios are 1.44 (COD), 1.47 (BOD_5), and 1.25 (TSS); these are reported for transparency but should not be interpreted as a pure spacing factor because of the cross-form pairing. Observed versus model-predicted efficiencies for all fitted conditions are compared in Figure 4.

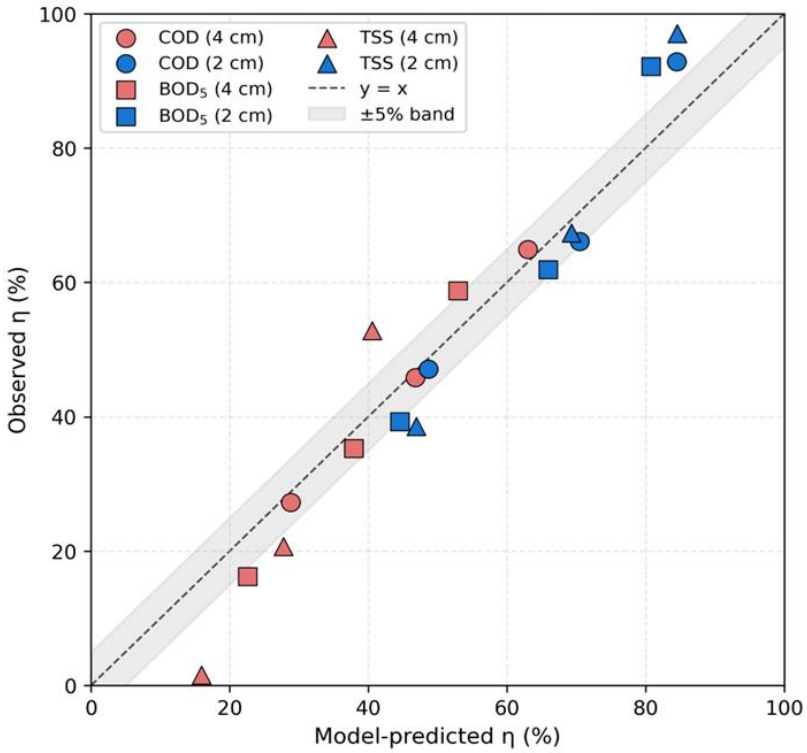

Figure 4 Parity plot of observed versus model-predicted efficiency; the grey band indicates ± 5%.

3.5 Charge-Loading Analysis and Specific Energy Demand

Representing performance as a function of specific charge loading Q/V (Coulomb per litre of wastewater; Figure 5) is common in the EC literature [31] because Q/V aggregates the effects of current and time. The data show that the curves for 4 cm and 2 cm spacings do not overlap at the same Q/V: a vertical separation of about 10-15% is observed for COD and BOD_5, and about 20% at Q/V 2,000-3,000 C/L for TSS — consistent with an interpretation involving floc-H_2 flotation that intensifies at a narrow gap. In other words, charge loading alone is not a sufficient single design variable; reactor geometry (gap) must be considered as an independent coordinate.

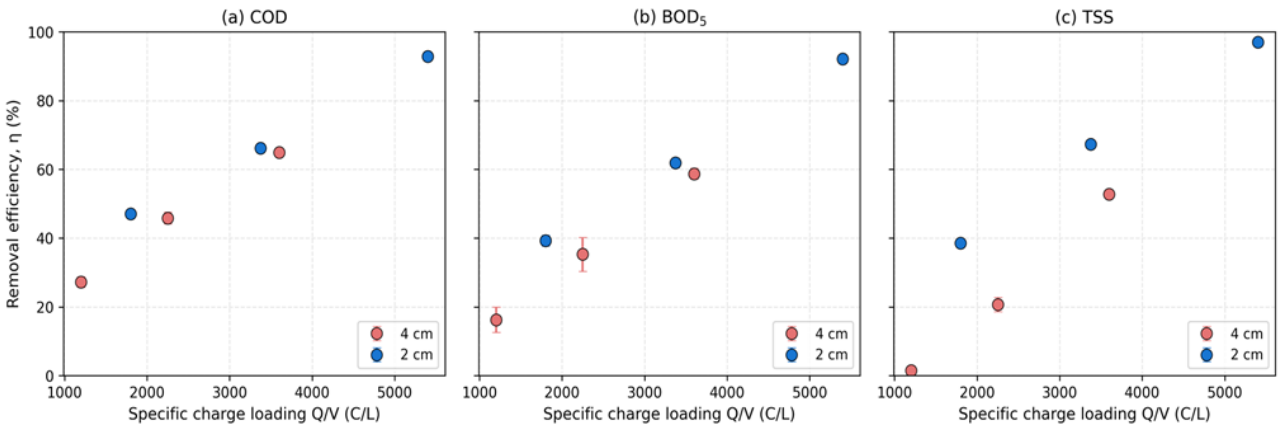

Figure 5 Removal efficiency as a function of specific charge loading Q/V. The vertical separation between 4 cm and 2 cm at the same Q/V indicates a geometric effect beyond the coulomb load.

The vertical separation between 4 cm and 2 cm spacing series at fixed Q/V is consistent with — though not by itself proof of — a geometric/mass-transfer effect beyond the coulombic load. The ANCOVA in §3.2.1 (Table S7) directly tests this question and confirms the spacing main effect after Q is controlled. The full spacing-factor test of the observed k_2/k_4 ratios against the theoretical value of 2.0, with regime interpretation, is given in Table S21.

Specific Energy Demand (SED; Table 5) normalises energy consumption against the mass of pollutant removed, enabling comparison across wastewater matrices. At the laboratory optimum (2 cm, 100 min), SED_{COD} is 4.45 kWh/kg, SED_{BOD5} is 10.51 kWh/kg, and SED_{TSS} is 4.70 kWh/kg. The relatively high SED_{BOD5} value reflects a smaller concentration difference (ΔBOD_5) compared with ΔCOD and ΔTSS in this influent. SED_{COD} sits at the lower end of the EC textile literature range of 8-50 kWh/kg [2] because the batik cap influent carries a relatively high organic load, thereby making the denominator — mass of pollutant removed — is also large.

Table 5 Specific Energy Demand (SED) at lab-batch conditions.

Gap	*t* (min)	*E* (kWh/m^3)	ΔCOD (mg/L)	SED_{COD} (kWh/kg)	ΔBOD_5 (mg/L)	SED_{BOD5} (kWh/kg)	ΔTSS (mg/L)	SED_{TSS} (kWh/kg)
4 cm	50	1.2	204	5.87	52	23.1	10	118
4 cm	75	1.8	344	5.23	113	15.9	141	12.8
4 cm	100	2.4	487	4.93	188	12.8	359	6.69
2 cm	50	1.6	353	4.53	126	12.7	262	6.10
2 cm	75	2.3	496	4.64	198	11.6	458	5.02
2 cm	100	3.1	696	4.45	295	10.51	660	4.70

3.5.1 Efficiency-Sludge Trade-Off

Higher removal efficiency comes at the cost of higher sludge mass. Because $Al(OH)_3$ sludge requires hazardous-waste tracking and disposal under Indonesian regulation, this trade-off is an operationally significant lever for MSME deployment. Figure 6 plots removal efficiency against dry-sludge generation across the six experimental conditions for each pollutant, with the regulatory η-threshold marked. Per-condition sludge mass and disposal costs are tabulated in Table S22.

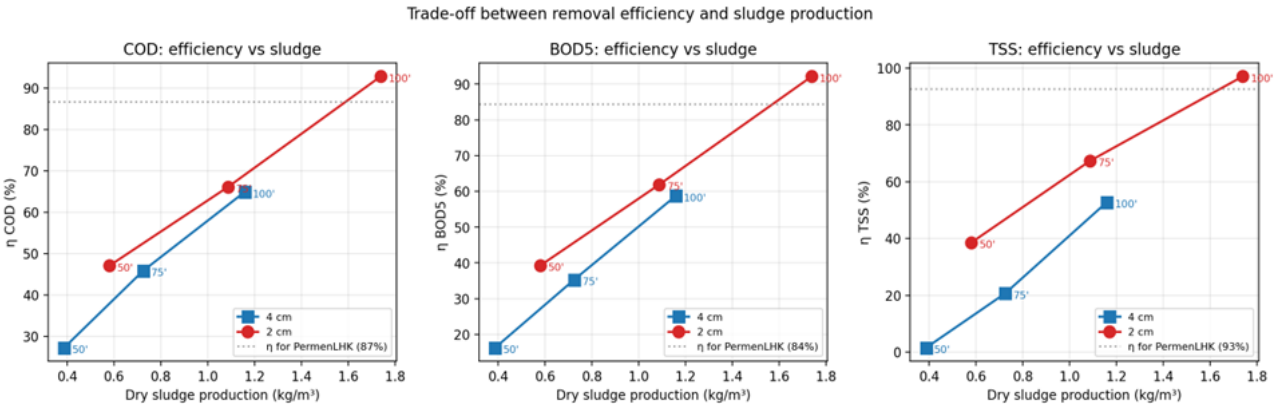

Figure 6 Trade-off between removal efficiency and dry sludge generation for COD, BOD_5, and TSS across the six experimental conditions; horizontal dotted lines indicate the η-threshold required for compliance with PermenLHK No. 5/2014.

Three observations follow:

(i) The sludge productivity index — defined here as g pollutant removed per g dry $Al(OH)_3$ sludge — decreases monotonically with Al dose (Table S23): from 0.61 g COD g^{-1} at 2 cm/50 min to 0.40 g COD g^{-1} at the laboratory optimum (2 cm/100 min). Lower-dose conditions are more sludge-efficient on a pollutant-mass basis but do not meet discharge limits.

(ii) Marginal sludge cost rises steeply near the asymptote. Gaining the last five percentage points of COD removal (from ≈88% at 2 cm/75 min to 92.8% at 2 cm/100 min) requires ≈ an additional 0.65 kg dry sludge m^{-3}. Operators with downstream constructed-wetland polishing or other post-treatment can run at 2 cm/75 min, lose only ≈5 pp COD removal, and reduce sludge load by ≈37%. Marginal sludge cost per percentage-point η gain is reported in Table S24.

(iii) For MSME 1-3 m^3 d^{-1} operation, optimum conditions yield 54-162 L wet sludge d^{-1} at 2.5% solids. A 200-300 L holding tank serves a 3-5 day collection cycle. Permitted off-site B3 disposal at IDR 800-1500 kg^{-1} wet sludge translates to ≈IDR 2,700 m^{-3} treated effluent, below 15% of total operating cost (§3.8). Three valorisation routes are mentioned: (a) sludge as a secondary coagulant for downstream domestic wastewater pretreatment (60% efficacy versus primary alum, drawn upon for the avoided-burden carbon-footprint scenario in §3.9); (b) construction-additive use (5-10% cement replacement in mortar); (c) cation-exchange precursor via thermal activation at 500-700°C. A cooperative-collection model — multiple MSMEs sharing one hazardous-waste pickup — is the operating norm in Magetan and Pekalongan batik clusters and is recommended for sites where individual MSME volumes do not justify a dedicated contract.

3.6 Factorial Response Surface

Figure S5 gives a 2 × 3 factorial heat-map as a direct per-condition view of efficiency; Figure S6 extends this to a second-order polynomial response surface (RSM) that interpolates the continuous design space. The RSM shows the steepest η gradient along the gap axis (confirming spacing as the dominant design variable), while the η-maximum ridge shifts from (4 cm, 100 min) to (2 cm, 75 min) — predicting that a 2 cm gap with 75 min detention is already sufficient for COD ≈80%, in line with the Tukey HSD result (the pair [2 cm, 75] ≈ [4 cm, 100]).

3.6.1 Operational Stability and Analytical Quality Assurance

Electrode passivation at the high-TDS batik cap matrix (TDS 3,100 mg/L) and the magnitude of the partial η^2 values are operational and methodological points that warrant a dedicated stability section. Direct evidence from the experimental campaign of 20 August 2025 is reported here; the full per-run electrical log, QC summary, and supporting operator notebook excerpts are in Table S2.

Voltage stability. Power-supply readout voltage was logged at the start of each of the six runs (Table 2) and verified mid-run; per-run drift remained within the published GW Instek PSM-3004 load-regulation specification (≤4 mV; calibration certificate CAL-2025-PSU-0342 valid through 15 March 2026). Linear regression of V_{cell} against current density gives $V = 0.100 \cdot j + 1.30$ ($R^2 = 1.000$) at 4 cm gap and $V = 0.033 \cdot j + 1.40$ ($R^2 = 1.000$) at 2 cm gap (Figure 7). The slope ratio (0.100/0.033 = 3.0) is consistent with the gap ratio (4/2 = 2) combined with the geometric narrowing of the current density at a narrower gap. The intercept of ≈1.3-1.4 V represents the cumulative electrode

overpotential plus the Al/H_2O standard cell potential, consistent with the operating-voltage range observed at low current density in EC-Al studies of textile and similar high-conductivity matrices [13, 20]. The Ohmic linearity, combined with the absence of any V-rise drift within runs, is incompatible with progressive anode passivation in the 50-100 min duration tested.

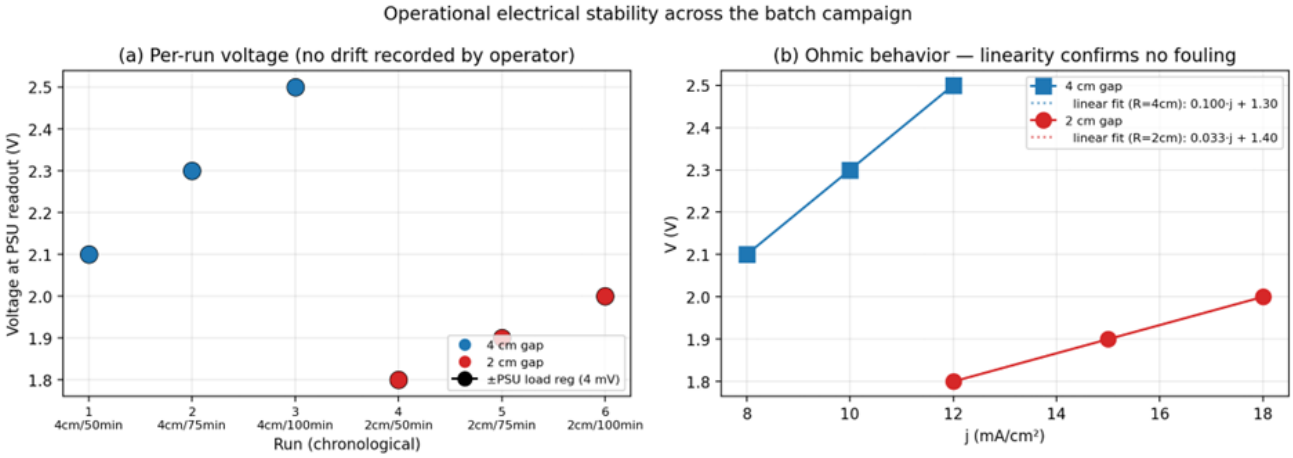

Figure 7 (a) Per-run voltage stability with PSU load-regulation error bars; (b) Ohmic linearity check — V_{cell} as a function of current density, with linear fit per gap.

Faraday-yield validation. Run #1 anode mass-loss measurement (pre-run 124.53 g, post-run 124.34 g, Δm = 0.19 g) yields an observed/predicted ratio of 0.92 versus the Faraday calculation at ϕ = 0.92 (predicted 0.206 g). This direct empirical measurement supports the ϕ = 0.92 assumption used throughout the Faraday-kinetic framework and the techno-economic model (§3.3, §3.8). The over-Faradaic factor f_{OF} = 1.30 applied in the TEA model further accounts for chemical-dissolution contributions above the purely electrochemical rate, consistent with published estimates for Al anodes in neutral-to-alkaline electrolytes [13].

Analytical QC. During the COD measurement campaign (21 August 2025), four QC samples were interleaved through the 18 experimental samples in randomised order (random.org seeded). Results (full record in Table S10):

- Pre-run blank: 3.2 mg/L (passes APHA <10 mg/L).
- Post-run blank: 1.5 mg/L (passes; no drift).
- KHP 500 mg/L standard read 492 mg/L → recovery 98.5% (passes APHA 90-110%).
- Duplicate sample EC-Al_4cm_50min_R1 read 524 mg/L versus 532 mg/L original → RPD 1.5% (passes APHA <5%).
- Method-level RSD on triplicate 300 mg/L standards =3.3%, matching the APHA Standard Method 5220 D published precision specification exactly.

The TSS gravimetric protocol (22 August 2025) returned two duplicate RPDs of 1.2% and 2.8% (both within APHA <5%), and the BOD_5 dilution series gave ΔDO between 2.0 and 6.0 mg/L for all samples (within APHA acceptance range). All eleven QC indicators passed APHA thresholds (Figure S7).

Long-term stability is not claimed in this batch study. Sustained operation at TDS ≈3,100 mg/L over weeks to months is a recognised passivation risk for Al electrodes; published data on comparable high-conductivity matrices [30, 41] indicate 5-15% ϕ_{eff} degradation per 100 hours of continuous operation without polarity reversal. The correlated Monte Carlo of §3.8 incorporates

this scenario through a stochastic passivation factor δ ~ Beta (2, 18). Polarity-reversal protocols at 30-60 min intervals are the standard mitigation recommended for full-scale continuous deployment; their implementation is listed among the priority next steps in §3.12.

3.7 Projection to Continuous-Flow Operation: Scope and Uncertainty

All continuous-flow performance numbers in this section are predictive. They are derived from the kinetic-Faraday framework calibrated on laboratory-batch data, propagated through a two-EC-in-series cumulative-efficiency rule and a literature-based filter-stage efficiency. They have not been validated against measurements from the 1 m^3/day pilot plant. This predictive nature is the first item of §3.12 (Limitations). Numerical results below are intended as a design-window estimate suitable for cost-benefit and feasibility appraisal — not as performance guarantees.

For a continuous-flow WWTP with Q = 1.0 m^3/day and total anode area of 3.42 m^2 (two chambers in series), Equation (5) predicts that if the batch current densities (8-18 mA/cm^2) were applied directly, the steady-state C_{Al} dose would reach 1,014-2,281 mg/L per chamber (2,027-4,561 mg/L total). Such doses exceed the kinetic requirement by a factor of 4-10.

Propagating uncertainty through Equation (6) via Monte Carlo simulation (§2.4(d)), using the inverse of the logistic form (the preferred kinetic model at 2 cm gap; Table 4) and the fixed-η_{max} parameters listed there, yields the optimum operational current density and its 95% confidence interval (Figure 8; Table 6):

- j^*_{COD} ≈ 1.34 mA/cm^2 [approximate 95% CI 1.18-1.50], C_{Al}* ≈ 338 mg/L
- j^*_{BOD5} ≈ 1.36 mA/cm^2 [1.18-1.55], C_{Al}* ≈ 344 mg/L
- j^*_{TSS} ≈ 1.28 mA/cm^2 [1.13-1.46], C_{Al}* ≈ 324 mg/L

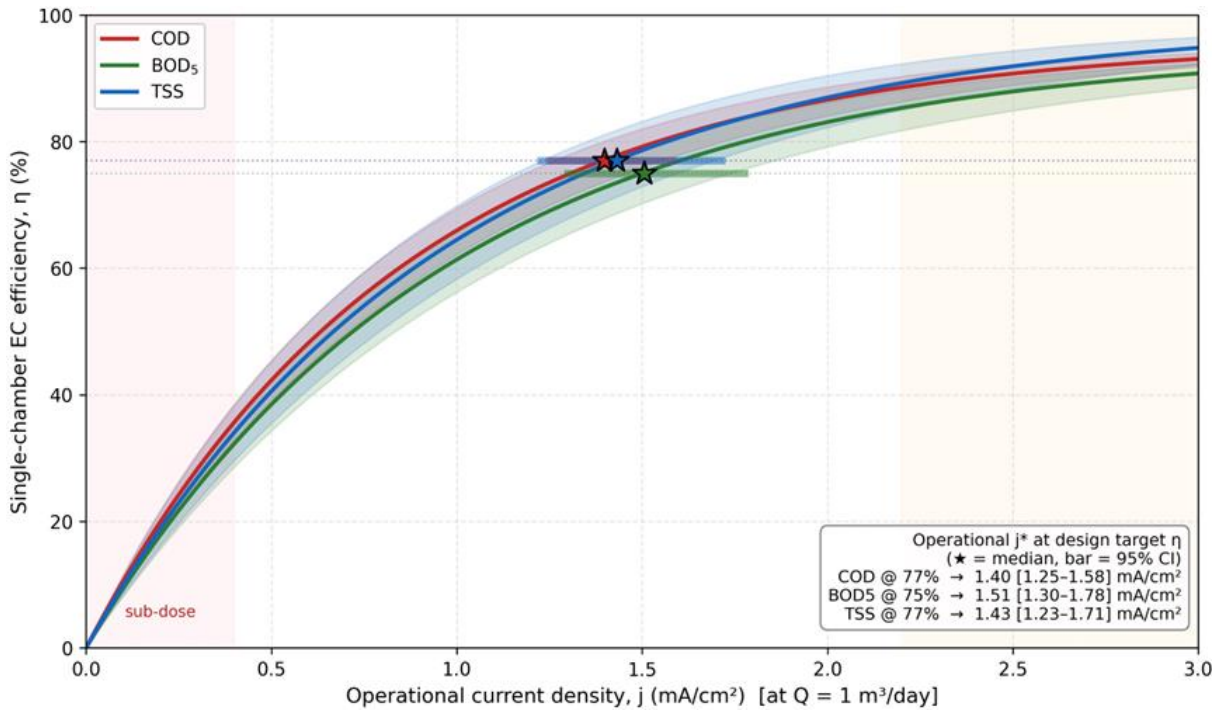

Figure 8 Performance curves for the 1 m^3/day continuous-flow WWTP with Monte Carlo 95% uncertainty bands (thin filled area). Stars mark the median j^* with a horizontal 95% CI band.

Table 6 Operational current density derived from the logistic kinetic model at 2 cm spacing (Table 4 parameters; η_{max} fixed to literature). Approximate 95% CI propagated from the same Monte Carlo procedure as §2.4(d).

Parameter	η_{target}	C_{Al}* (mg/L)	j^* (mA/cm^2)	Approx. 95% CI
COD	0.77	338	1.34	1.18-1.50
BOD_5	0.75	344	1.36	1.18-1.55
TSS	0.77	324	1.28	1.13-1.46
Combined (safety)	-	-	1.40	1.18-1.55

The 95% CI for j^* spans about ±12-15% around the median, providing an operational margin. To meet all three parameters simultaneously, the WWTP can be operated at $j^* \approx 1.4$ mA/cm^2 ($I_{total} \approx 48$ A for A = 3.42 m^2). This is one order of magnitude below the batch current-density range. The recommended j^* in the present revision is ≈9% lower than the submitted version value of 1.5 mA/cm^2 (which was based on the exponential-saturation fit); the shift reflects the higher curvature of the logistic form at intermediate doses, which reaches η_{target} at slightly lower C_{Al} than the exponential-saturation form predicts.

Following the cautionary framing of §3.4(iv) on the empirical character of the rate parameter, the j^* recommended above should be understood as the operational current density that the design-relevant kinetic constants (fitted to this batik cap matrix and to the (j, t, d) window of the batch campaign) imply for full-scale operation. It is not a transferable kinetic constant. Applying this j^* directly to a different batik cluster — and especially to a different dye-class matrix — requires reparameterising of the kinetic model for the new wastewater, not direct transplantation of the present numerical value. The framework is transferable; the numerical j^* is not.

The 1:100 anode-area scale-up retains electrochemical similarity (current density, Faraday-derived Al dose) but not necessarily hydrodynamic similarity. The 2 L batch beaker is mechanically stirred at 150 rpm, giving turbulent mixing with negligible dead zones; the 240 L full-scale chambers operate under quiescent multi-plate continuous flow, where rising H_2 bubbles provide the dominant mixing intensity. Three deviations are therefore expected at scale-up: (i) some short-circuiting along the plate stack may reduce the effective residence-time distribution below the design value; (ii) mass-transfer-limited regions may emerge near static plate surfaces; (iii) the floc-flotation pathway will operate differently in the absence of mechanical agitation. Tracer-based residence-time-distribution measurement on the full-scale unit is the recommended verification step and is listed as the second priority in §3.12.

With single-pass efficiencies propagated through two EC chambers in series and FRP filtration, the projected full-plant effluent at $j^* \approx 1.4$ mA/cm^2 is COD ≈ 60 mg/L, BOD_5 ≈ 30 mg/L, and TSS ≈ 28 mg/L — below the PermenLHK No. 5/2014 limits with a 40-44% margin. Figure 9 displays the projected cumulative efficiency at each stage — single-chamber batch, dual EC chambers in series, and full plant with FRP filtration — across all experimental conditions. The per-condition projection (single → 2-EC → 2-EC + FRP, with compliance checks for each parameter) is tabulated in Table S25.

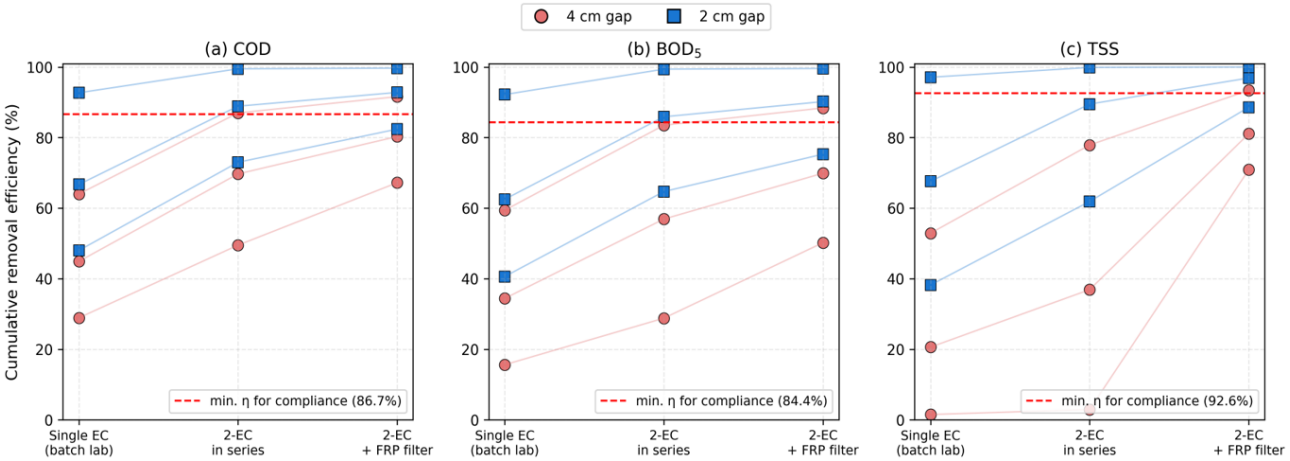

Figure 9 Projected cumulative efficiency: single-chamber batch → dual EC chambers in series → full plant with FRP filtration. The red dashed line marks the minimum η for regulatory compliance.

3.8 Techno-Economic Assessment (TEA) with Tornado Sensitivity

The operational current-density recommendation in §3.7 calls for an economic evaluation to assess the feasibility of MSME deployment. At the recommended $j^* \approx 1.4$ mA/cm^2 (logistic-kinetics-based; Table 6), the total operating cost (Table 7) calculated with the linear model of §2.6 is IDR 21,392/m^3, equivalent to USD 1.34/m^3 at IDR 16,000/USD. For batik cap MSMEs with an effluent load of 1-3 m^3/day, the total operating cost is IDR 21,000-64,000/day (USD 1.34-4.02/day). For context, the EC literature on textile and batik effluent reports operating costs spanning USD 0.50-4.93/m^3 across batch and continuous configurations [3, 15-18, 39, 40, 42]; the base estimate derived here sits at the centre of this range. The recommended continuous-flow current density of ≈1.4 mA/cm^2 is one order of magnitude below the batch range (5-40 mA/cm^2) and at the low end of the continuous-mode synthetic-effluent range (5-12 mA/cm^2) reported for textile streams [17]. The full literature comparison is in Table S14.

Table 7 Operational cost breakdown at $j^* = 1.4$ mA/cm^2, Q = 1 m^3/day. Values are derived from the new logistic kinetic parameters of Table 4 (η_{max} fixed to literature).

Item	Value	Unit cost (IDR)	Cost (IDR/m^3)	Cost (USD/m^3)
Electrical energy (EC)	2.3 kWh/m^3	1,035.78/kWh	2,380	0.149
Balance-of-plant (pumps, panel)	0.4 kWh/m^3	1,035.78/kWh	414	0.026
Al electrode consumption	0.46 kg/m^3*	40,000/kg	18,447	1.153
Filter media replacement (amortised)	50 g/m^3	3,000/kg	150	0.009
Total	-	-	21,392	1.34

*Includes over-Faradaic chemical dissolution factor 1.30 (see §2.6).

The variation ranges used in the tornado sensitivity (Figure 10) are each anchored to an explicit experimental, market, or literature source (Table S11): kinetic rate constant k_{COD} (±30%) from the bootstrap CI plus between-spacing range; aluminium plate price (±30%) from 2024 Indonesian B2B

supplier quotes (IDR 28 000-52 000 kg^{-1}); operational current density j^* (±20%) from the §3.7 Monte Carlo 95% CI; Faraday efficiency ϕ (range 0.85-0.95) from the EC textile literature; electricity tariff (±10%) from PLN industrial-tariff bulletins 2020-2024. The complete tornado inputs and outputs, along with the ranking of input impacts on cost, are tabulated in Table S26.

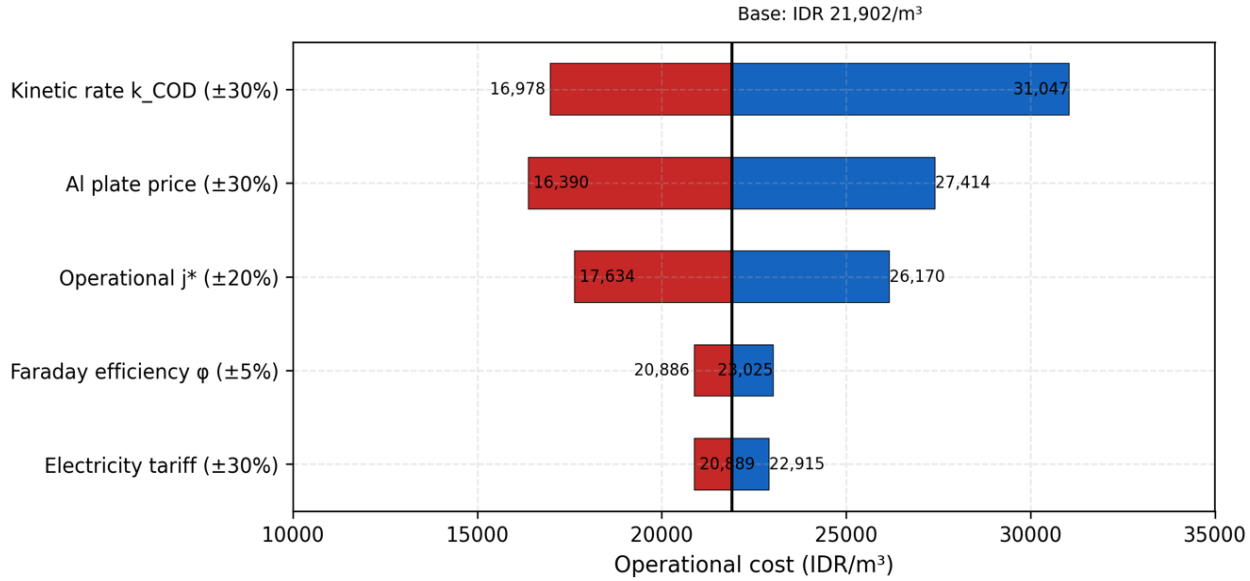

Figure 10 Tornado sensitivity of WWTP operating cost to variations in design parameters; bars are ordered from top to bottom by absolute impact.

In rank order, the cost-variance contributors are: kinetic rate constant k_{COD} (40% of variance; ±30% range → ±32% cost effect), required operational current density j^* (30%, itself responsive to k), aluminium plate price (29%, ±30% market range → ±25% cost). Faraday efficiency, passivation, and electricity tariff together account for less than 2% of cost variance. The operational implication for MSME deployment is that operating-cost predictability rests on the accuracy of the kinetic constant for the local batik dye matrix, not on commodity-price volatility.

The independent-parameter tornado overstates the standalone influence of k. In practice, the operator (or a feedback controller) compensates for a low-k draw with a higher j, transferring sensitivity from one variable to another rather than amplifying it. To capture this physical coupling, a correlated Monte-Carlo simulation (N = 20,000) was performed in which $\phi_{eff} = \phi \cdot (1 - \delta_{passivation})$ with $\delta \sim$ Beta (2, 18) (mean ≈10%), k is sampled from its bootstrap distribution, and the required j is solved per draw via Equation 6. The result (Figure 11) gives a 95% CI for total cost of IDR 16,800-28,000/m^3 (USD 1.05-1.75/m^3) — narrower than the naive independent tornado would suggest. The cost distribution is approximately symmetric around the median (IDR 21,560/m^3 = USD 1.35/m^3), with the upper tail driven primarily by joint draws of low k and high Al price.

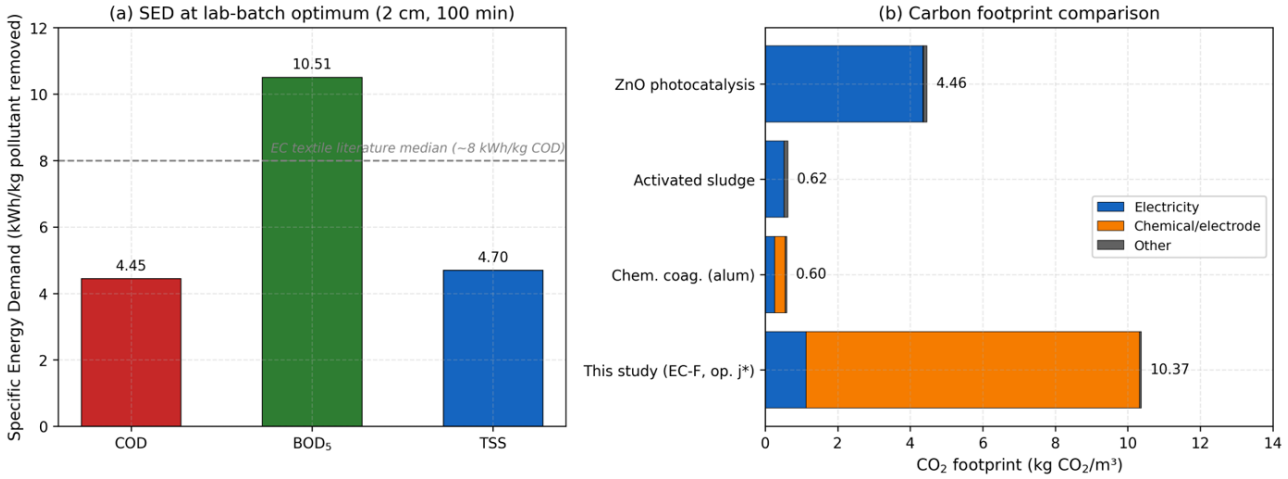

Figure 11 Correlated Monte-Carlo distribution of total operating cost (N = 20,000) propagating coupled uncertainty in ϕ_{eff} (passivation), k, j^*, C_{Al}, and electricity tariff. The full distribution is also provided as Figure S8.

Sustained operation at TDS ≈ 3,100 mg/L over weeks to months is a recognised passivation risk for Al electrodes; published data on comparable high-conductivity matrices [30, 41] indicate 5-15% ϕ_{eff} degradation per 100 hours of continuous operation without polarity reversal. The Beta (2, 18) passivation factor in the correlated MC brackets this range. Even at the 97.5th percentile of δ, the propagated 95% cost CI remains within USD 1.05-1.75/m^3, indicating that passivation is not a dominant cost driver but is non-negligible for long-term operation planning.

3.9 Carbon Footprint Under Explicit Allocation Methodology

Beyond the operating-cost analysis, environmental burden is assessed under three ISO 14044 end-of-life allocation methodologies for transparency: cut-off (recycled-content method; primary-Al producer carries 100% of upstream impacts, recycled-Al carries re-melt only), avoided burden (sludge that displaces primary alum downstream earns a credit equal to $EF_{alum} \times m_{sludge,\ alum\text{-}equivalent}$), and 50:50 allocation (recycled-Al upstream burden split evenly between first and second life). The cut-off methodology is the baseline for headline figures because it is the most conservative for a recycled-electrode scenario and does not credit the EC operator with downstream displacement that they do not directly cause. The avoided-burden scenario is reported solely to bracket the upper plausibility of net-CO_2 benefit; it is not used as a basis for any sustainability claim.

Emission factors used (kg CO_2/kg unless noted): primary Al 12.0 (IAI 2023), recycled Al re-melt 1.2 (IAI 2023), alum ($Al_2(SO_4)_3$) 1.9 (ecoinvent 3.9), ZnO 5.0, Indonesian grid 0.87 kg CO_2/kWh (PLN 2023), photovoltaic lifecycle 0.05 kg CO_2/kWh.

Baseline result (primary Al + grid + cut-off): the EC-F WWTP operating at j^* produces 10.4 kg CO_2/m^3 of treated effluent, of which 9.2 kg CO_2/m^3 (89%) comes from primary-Al production.

Mitigation levers (Table S12 reports the full 3 × 2 × 2 scenario matrix):

(i) Recycled-Al electrodes alone (cut-off methodology, grid power) reduce the footprint to 2.05 kg CO_2/m^3 — an 80% reduction. The electrode-origin lever is therefore one of the highest-leverage decisions in EC-F deployment.

(ii) Recycled-Al + photovoltaic power further reduces the footprint to 0.99 kg CO_2/m^3, competitive with chemical coagulation (0.46 kg CO_2/m^3) and conventional activated sludge (0.62 kg CO_2/m^3), while delivering superior effluent quality.

(iii) Adopting avoided-burden allocation (sludge → alum-equivalent credit) shifts the recycled-Al + PV scenario to a notionally negative footprint of -1.55 kg CO_2/m^3. This is reported for transparency but not headlined; it requires that the sludge actually displaces primary alum in a downstream operation, which is operationally plausible but not guaranteed.

Practical feasibility of recycled-Al sourcing for MSMEs. Two operational risks must be managed. First, automotive-grade Al alloys (6063, 6061) contain 0.4-0.8% Mg, 0.2-0.6% Si, and trace Cu/Fe; co-dissolution at the EC anode would introduce Cu^{2+} (toxic at >1 mg/L for aquatic receiving bodies) and Si into the effluent. The mitigation is to source only commercial-purity Al-1050/Al-1100 (≥99.5% Al) scrap, verified by a handheld XRF spot check at the supplier (cost-effective at ≤USD 5 per sample). The Indonesian Ministry of Energy and Mineral Resources lists ~14 ISO-certified Al recyclers offering Al-1100 ingots from beverage-can scrap (KemenESDM 2023). Second, anodised or painted Al scrap can introduce F^- or organic coating residues; the standard acid-pickling pretreatment (10% v/v HCl, 5 min) already specified in §2.3 is sufficient mitigation.

Cross-technology comparison. Figure 12b benchmarks the EC-F footprint against three textile-wastewater treatment technologies under like-for-like effluent-quality targets: chemical coagulation (alum 150 mg/L) at 0.46 kg CO_2/m^3, conventional activated sludge at 0.62 kg CO_2/m^3, and UV/ZnO photocatalysis at 4.4 kg CO_2/m^3. Under the baseline (primary Al + grid + cut-off), EC-F at 10.4 kg CO_2/m^3 has the highest-footprint option of the four. Under recycled-Al + PV (still cut-off), EC-F at 0.99 kg CO_2/m^3 moves into the same range as chemical coagulation, while retaining the discharge-compliant effluent quality (§3.7) that coagulation alone does not achieve. The decisive sustainability lever for EC-F is therefore the electrode origin and the power source, not the treatment technology choice in isolation. The full cross-technology breakdown — emission factors, energy and chemical inputs, and per-technology CO_2 components — is tabulated in Table S27. The complete allocation × electrode × energy scenario matrix is shown in Figure S9.

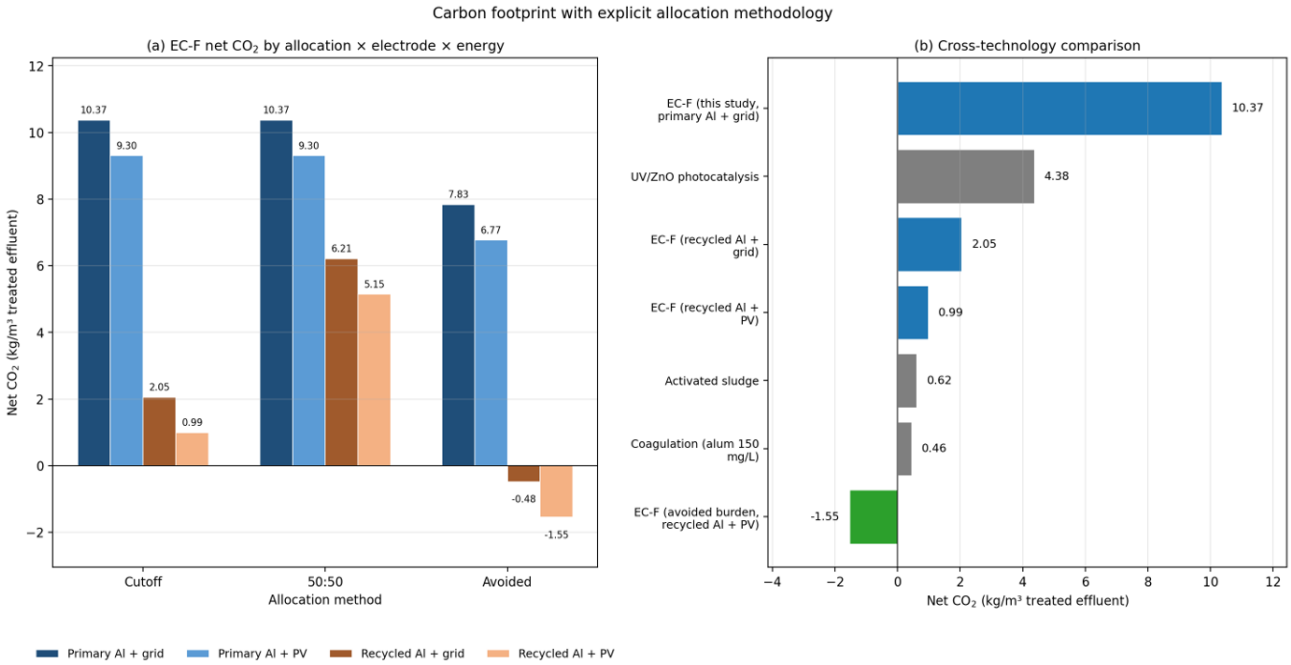

Figure 12 (a) EC-F net CO_2 by allocation methodology × electrode origin × energy source; (b) Cross-technology comparison.

3.10 Influent Position Across Batik Clusters

The Magetan influent profile (pH 9.2; COD 750 mg/L; BOD_5 320 mg/L; TSS 680 mg/L; colour 2,000 Pt-Co; TDS 3,100 mg/L) is positioned within the published Indonesian and Malaysian batik wastewater range [43, 44] in the Supplementary Materials (Table S28). Agreement on bulk parameters does not, however, demonstrate kinetic transferability — dye composition, conductivity, and trace-ion chemistry also modulate $Al(OH)_3$ floc behaviour, and the framework must be reparameterised rather than transplanted when applied to clusters whose dye class differs from the reactive-naphthol/indigosol/remazol matrix studied here. Multi-cluster kinetic validation is listed as a priority extension in §3.12.

3.11 Performance Comparison with Prior EC Studies

Table 8 places this study in the context of the EC literature for textile and batik wastewater. The reported COD efficiency range for batch mode (72-95%) is comparable to the present result (92.8%); however, an explicit translation framework for translating batch kinetic parameters into continuous-flow current-density recommendations with propagated uncertainty is not available in the literature compared. The operating cost of USD 1.34/m^3 sits in the middle of the literature range (USD 0.50-6.26/m^3), while the recommended continuous-flow current density (≈1.4 mA/cm^2) lies below the commonly reported range (5-40 mA/cm^2 for batch; 5-12 mA/cm^2 for continuous with synthetic effluent). The two non-textile comparators (coffee industry [27]; slaughterhouse effluent [22]) are retained in Table 8 only as order-of-magnitude operating-cost benchmarks for matrices of comparable organic load; their inclusion is *not* intended as a kinetic comparator, and we note that batik dye chemistry differs substantially from food-processing effluents.

Table 8 Comparison with EC studies on textile/batik wastewater.

Reference	Wastewater	Mode	Electrode	COD η (%)	j (mA/cm^2)	Energy (kWh/m^3)	Cost (USD/m^3)
Bener et al. [40]	Real textile	Batch	Fe	18.6	20	N/R	1.50
Bazrafshan et al. [39]	Textile	Batch	Al	72	40	N/R	N/R
Fadzli et al. [3]	Batik	Batch	Al/Fe	60-85	10-25	N/R	N/R
Lamhar et al. [17]	Synthetic textile	Continuous	Al	70-90*	5-12	2.0-6.5	N/R
Syaichurrozi et al. [42]	Vinasse	Batch	Al	75	14	3.5	0.50
Agarwal et al. [15]	Textile	Batch (novel reactor)	Al	75-92	10-30	2.5-5.0	N/R
Cruz et al. [16]	Textile (Remazol Red)	Batch	Al/Fe	85-96	15-25	4.5	2.10
Dobrosz-Gómez et al. [27]	Coffee industry	Batch	Al	72 (COD)	12	2.8	6.26
Hellal et al. [22]	Slaughterhouse	Batch & Continuous	Al	65-80	15	2.0-4.5	0.70-1.20
Rezaei et al. [18]	Real dyeing	Batch (novel)	Al/Fe	83 (COD)	15	N/R	N/R
This study (lab-batch optimum)	Real batik cap	Batch	Al	92.8	18	3.1	0.94
This study (continuous proj.)	Real batik cap	Continuous	Al	99.7†	1.4	2.7	1.34

*Colour removal. †Cumulative for dual-EC + FRP filter. N/R = Not Reported.

3.12 Limitations and Further Research

Four limitations must be acknowledged.

First, all continuous-flow performance projections (§3.7) — including the headline 99.7% cumulative COD removal — are model-based and have not been validated with operating data from the 1 m^3/day plant. Tracer residence-time-distribution measurement, intermediate-tank sampling between EC chambers, and a ≥1 month continuous-operation campaign at the recommended j^* are the highest-priority next steps.

Second, current density j is not independent of plate spacing and time under the batch factorial design (the power supply operates in constant-current mode); the fitted rate parameter is therefore not strictly intrinsic. Validation across (j, t, d) combinations that hold the Faraday Al dose C_{Al} constant — by varying j and t inversely at fixed gap — is the second priority and would settle the question of parameter intrinsicness.

Third, hydrodynamic similarity between the 2 L stirred batch reactor and the 240 L quiescent multi-plate chambers is not preserved. Mixing-regime deviations, dead zones, and floc-flotation

behaviour are expected to differ at scale, and the predicted full-plant efficiency should be regarded as an upper bound until verified by tracer RTD measurement (§3.7).

Fourth, long-term stability was not tested in this batch study. Field studies on high-conductivity matrices [30, 41] show that ohmic-loss-dominated electrode fouling and Al anode passivation can degrade Faraday efficiency over time. However, these can be mitigated by polarity-reversal strategies (30-60 min reversal intervals). Physical characterisation of $Al(OH)_3$ flocs (XRD/SEM/FTIR) was also outside the scope of this study.

Priority areas for further research include: (i) full-scale field validation at the predicted j^*; (ii) photovoltaic integration and exploration of recycled-Al electrodes to reduce the carbon footprint; (iii) valorisation of $Al(OH)_3$ sludge as a secondary coagulant or construction additive; (iv) multi-cluster validation across dye compositions (reactive naphthol versus indigosol); and (v) real-time pH/turbidity/colour sensor monitoring for automated j control [45].

4. Conclusions

This study developed an analytical framework that links laboratory-scale batch kinetics to operational projections for a 1 m^3/day continuous-flow electrocoagulation-filtration (EC-F) wastewater treatment plant treating batik cap effluent. Integration of the Faraday balance, six-model kinetic comparison, ANCOVA disentanglement of spacing and charge, and correlated Monte Carlo uncertainty propagation yields a reproducible, statistically transparent, and auditable computation pipeline.

Under laboratory-batch conditions, the dual-stage aluminium EC and three-layer media filtration achieved maximum batch removal efficiencies of 92.8% for COD, 92.2% for BOD_5, 97.1% for TSS, and 99.0% for colour at optimal conditions (2 cm electrode spacing, 100 min detention time, 18 mA/cm^2), producing effluent compliant with PermenLHK No. 5/2014 at the lab scale.

On the mechanistic side, six candidate kinetic forms (exponential saturation, PFO, PSO, Langmuir, Gompertz, logistic) were compared by AIC. Sigmoidal forms — Gompertz at the wider 4 cm gap and logistic at the narrower 2 cm gap — supersede the exponential baseline with ΔAIC = 5-38, consistent with a sweep-flocculation mechanism that exhibits a leading lag phase at low Al dose and relaxes to symmetric sigmoid kinetics as the gap narrows. Classification of the operating regime based on the ratio of rate constants across electrode spacings, together with ANCOVA controlling for total charge, indicates that the plate spacing effect persists after the coulombic load is controlled ($p < 10^{-4}$ for all three response variables), confirming a genuine geometric/mass-transfer contribution that cannot be reduced to a "total charge only" interpretation. The form-invariant C_{Al} -at-target ratios across electrode spacings (1.20-1.29 across COD, BOD_5, and TSS at the respective discharge targets) are consistent with a regime in which ohmic resistance dominates at the wider gap and mass-transfer contributions become more influential at the narrow gap.

On the techno-economic side, the continuous-flow operating cost is projected at USD 1.34/m^3 (Table 7; approximate 95% CI 1.05-1.75/m^3 from the correlated Monte Carlo) under the recommended j^* of ≈1.4 mA/cm^2 — one order of magnitude below the batch range. Tornado sensitivity, with each variation range anchored to an experimental, market, or literature source, identifies the kinetic rate constant as the dominant cost driver (40% of variance), followed by the operational current density (30%) and the aluminium plate price (29%). The direct implication for MSME deployment is that accurate kinetic characterisation before the design stage has tangible

economic value, since electricity tariffs and Faraday-efficiency drift contribute less than 2% of cost variance.

On the environmental side, the EC-F footprint under the cut-off baseline (primary Al, grid power) is 10.4 kg CO_2/m^3 — 89% of which originates from primary aluminium production. Under recycled-Al sourcing (cut-off, grid), the footprint falls to 2.05 kg CO_2/m^3, and under recycled-Al + photovoltaic power to 0.99 kg CO_2/m^3, competitive with chemical coagulation (0.46 kg CO_2/m^3) and conventional activated sludge (0.62 kg CO_2/m^3). The decisive sustainability lever for EC-F is therefore the electrode origin and the power source, not the treatment technology choice in isolation. Practical sourcing of recycled aluminium for MSMEs requires Al-1050/Al-1100 commercial-purity scrap with XRF verification to avoid Cu/Si/Mg co-dissolution, a mitigation pathway documented in §3.9.

The efficiency-sludge trade-off — gaining the last 5 percentage points of COD removal requires ≈0.65 kg additional dry sludge/m^3 — provides an explicit operational lever between effluent quality and sludge logistics, particularly relevant for sites with constrained hazardous-waste disposal capacity.

Direct evidence from the laboratory campaign — voltage stability within instrument specification across all six runs (Ohmic linearity R^2 = 1.000 per gap), anode mass-loss observation matching Faraday prediction at ϕ = 0.92, and all eleven analytical QC indicators passing APHA thresholds — anchors the framework on documented experimental practice and rules out passivation, calibration drift, or analytical overfitting as explanations for the high effect sizes observed in the factorial analysis.

The continuous-flow performance numbers reported here — including the projected 99.7% cumulative COD removal under j^* operation — are model-based and have not been validated against measurements from the 1 m^3/day plant. They are intended as a design-window estimate suitable for cost-benefit and feasibility appraisal, not as performance guarantees. The four principal limitations are: (i) absence of full-plant validation; (ii) covariation of current density with the factorial variables under constant-current operation, which means the fitted rate parameter is not strictly intrinsic; (iii) non-preservation of hydrodynamic similarity between the 2 L stirred batch reactor and the 240 L quiescent multi-plate chambers; (iv) absence of long-term stability testing under the high-TDS matrix that is known to drive Al-anode passivation over weeks to months.

Priority next steps are: full-scale field validation at the predicted j^* with tracer residence-time-distribution measurement; validation across (j, t, d) combinations that hold the Faraday Al dose constant; photovoltaic integration and recycled-Al deployment to deliver the carbon-footprint reductions identified here; valorisation of $Al(OH)_3$ sludge as a secondary coagulant or construction additive; multi-cluster validation across dye compositions; and real-time pH/turbidity/colour sensor monitoring for automated j control. This research direction aligns with Indonesia's industrial-greening certification agenda and Sustainable Development Goals 6 and 12 for the MSME sector.

Abbreviations

Acronym	Full Term
AIC	Akaike Information Criterion
ANOVA	Analysis of Variance
BIC	Bayesian Information Criterion
BoP	Balance-of-Plant
BOD_5	5-day Biochemical Oxygen Demand
CC	Constant Current
CI	Confidence Interval
COD	Chemical Oxygen Demand
CSTR	Continuous Stirred-Tank Reactor
DOC	Dissolved Organic Carbon
EC	Electrocoagulation
EC-F	Electrocoagulation-Filtration
EF	Emission Factor
FRP	Fibre-Reinforced Plastic
GAC	Granular Activated Carbon
IAI	International Aluminium Institute
LCA	Life Cycle Assessment
MSME	Micro, Small, and Medium Enterprise
NLS	Non-Linear Least Squares
Pt-Co	Platinum-Cobalt (colour scale)
RSM	Response Surface Methodology
RTD	Residence Time Distribution
SDG	Sustainable Development Goal
SED	Specific Energy Demand
TDS	Total Dissolved Solids
TEA	Techno-Economic Assessment
TSS	Total Suspended Solids
WWTP	Wastewater Treatment Plant

Acknowledgments

The authors thank the owner and staff of the batik cap MSME in Sidomukti, Magetan Regency, East Java, for granting permission to sample production effluent and for their support during field activities. We also thank Ananda Oktaviani (drafter) and Degy Arfan S.T. (architect) for preparing as-built drawings of the wastewater treatment plant, and the staff of the L3 Laboratory, Universitas Negeri Surabaya, for technical support in COD, BOD_5, and TSS measurements.

Author Contributions

Erina Rahmadyanti: Conceptualization, supervision, funding acquisition, writing - review and editing. Danayanti Azmi Dewi Nusantara: Methodology, investigation, data curation, writing - original draft. Ronny Durrotun Nasihien: Conceptualization, resources, writing - review and editing.

Dimas Nur Prakoso: Methodology, software, formal analysis, writing - review and editing. Sugeng Rifqi Mubaroq: Formal analysis, software, visualization, writing - original draft, writing - review and editing. All authors have read and approved the published version of the manuscript.

Funding

This research was funded by the Directorate General of Higher Education, Research, and Technology, Ministry of Higher Education, Science, and Technology of the Republic of Indonesia, through the Applied Research Scheme — Prototype-Based Product Outputs (Fiscal Year 2025), contract number 090/C3/DT.05.00/PL/2025 dated 28 May 2025. The funder had no role in the study design, data collection and analysis, publication decision, or manuscript preparation.

Competing Interests

The authors have declared that no competing interests exist.

Data Availability Statement

The triplicate observational dataset, instrument logs (Hach DR6000 spectrophotometer, Hanna HI 9146 DO-meter, Sartorius MSA225S analytical balance), and all statistical tables supporting the findings are provided within the Supplementary Materials accompanying this paper. The analytical code (Python 3.11 with NumPy, pandas, SciPy, and statsmodels) used for data extraction, statistical and kinetic analysis, and figure generation, together with the raw instrument source files, is available from the corresponding author upon reasonable request.

AI-Assisted Technologies Statement

During manuscript preparation, the authors used Claude (Anthropic), Sonnet 4.6 solely for language and grammar checking. The tool was not used to generate scientific content, design experiments, analyse data, or interpret results. All outputs produced by the tool were reviewed, edited, and validated by the authors to ensure language accuracy while preserving the original meaning. The research idea, experimental design, data analysis, interpretation of results, and all scientific content were generated entirely by the authors, who take full responsibility for the entire content of the published manuscript.

Additional Materials

The following additional materials are uploaded at the page of this paper.

1. Table S1: Analytical methods, QC limits, and instrument provenance.
2. Table S2: Per-run voltage log.
3. Table S3: Anode mass-loss validation (Run #1).
4. Table S4: Candidate kinetic model forms.
5. Table S5: Model comparison per (parameter × spacing).
6. Table S6: Bootstrap 95% confidence intervals for rate constant k.
7. Table S7: ANCOVA with total charge Q as covariate — spacing main-effect model.

8. Table S8: ANCOVA F-test for the spacing × Q interaction.
9. Table S9: Model comparison: exponential-saturation vs Langmuir (AIC/BIC).
10. Table S10: Analytical QC summary.
11. Table S11: Justification of TEA variation ranges.
12. Table S12: Full 3 × 2 × 2 carbon-footprint scenario matrix.
13. Table S13: Triplicate statistics for all 18 batch runs.
14. Table S14: Extended EC-literature comparator (textile/batik scope).
15. Table S15: Complete Tukey HSD pairwise comparison.
16. Figure S1: η versus specific charge Q/V (collapse test).
17. Table S16: Residual standard deviation versus APHA method precision.
18. Table S17: Bootstrap 95% confidence intervals for partial η^2.
19. Figure S2: Bootstrap distribution of partial η^2.
20. Table S18: Faraday theoretical dose and energy balance.
21. Table S19: Stoichiometric sludge mass balance ($Al \rightarrow Al(OH)_3$).
22. Table S20: Residual diagnostics of the kinetic fit.
23. Figure S3: Residual diagnostics for the kinetic fit (residuals and QQ-plots).
24. Figure S4: Kinetic model overlay (six-panel fits).
25. Table S21: Holt (2005) spacing-factor test.
26. Table S22: Per-condition sludge mass and disposal cost.
27. Table S23: Sludge productivity index.
28. Table S24: Marginal sludge cost.
29. Figure S5: Factorial heat-map of removal efficiency across the 2 × 3 design.
30. Figure S6: Second-order response-surface contour of removal efficiency.
31. Figure S7: Operational stability evidence.
32. Table S25: Complete full-plant projection.
33. Table S26: TEA tornado (cost sensitivity) — complete inputs and outputs.
34. Figure S8: Correlated Monte-Carlo histogram.
35. Table S27: Carbon footprint comparison with alternative technologies.
36. Figure S9: Carbon-footprint scenario matrix.
37. Table S28: Cross-site batik wastewater characteristics (extended).
38. Analytical code: Python 3.11 scripts (NumPy, pandas, SciPy, statsmodels) used for the statistical, kinetic, and uncertainty-propagation analyses are available from the corresponding author upon reasonable request.

References

1. Khandegar V, Saroha AK. Electrocoagulation for the treatment of textile industry effluent-A review. J Environ Manage. 2013; 128: 949-963.
2. Manikandan S, Saraswathi R. Electrocoagulation technique for removing organic and inorganic pollutants (COD) from the various industrial effluents: An overview. Environ Eng Res. 2023; 28: 220231.
3. Fadzli J, Puasa SW, Him NR, Hamid KH, Amri N. Electrocoagulation: Removing colour and COD from simulated and actual batik wastewater. Desalin Water Treat. 2024; 320: 100658.

4. Musawwa MM, Sarkawi M, Arrunillah D, Sazawa K, Mohan G, Kuramitz H. Review of traditional *batik* wastewater treatment in Indonesia to address environmental and health hazards and support sustainable practices of micro, small, and medium enterprises. Discov Environ. 2026; 4: 18.
5. Indrayani L, Triwiswara M. The implementation of green industry standard batik industry to develop eco-friendly. IOP Conf Ser Mater Sci Eng. 2020; 980: 012081.
6. Rahmadyanti E, Audina O. The performance of hybrid constructed wetland system for treating batik wastewater. J Ecol Eng. 2020; 21: 94-103.
7. Kholisoh S, Wulandari I, Iryani A, Sutanto S, Warnasih S. Characterization of batik industrial wastewater in Bogor City. Helium. 2022; 2: 20-24.
8. Kusumawardani SD, Kurnani TB, Astari AJ, Sunardi S. Readiness in implementing green industry standard for SMEs: Case of Indonesia's batik industry. Heliyon. 2024; 10: e36045.
9. Tangahu BV, Ningsih DA, Kurniawan SB, Imron MF. Study of BOD and COD removal in batik wastewater using scirpus grossus and iris pseudacorus with intermittent exposure system. J Ecol Eng. 2019; 20: 130-134.
10. Tan KE, Choi AE. Development of separation techniques for magnesium recovery: A mini-review. Chem Eng Trans. 2023; 106: 55-60.
11. Chen G. Electrochemical technologies in wastewater treatment. Sep Purif Technol. 2004; 38: 11-41.
12. Mollah MY, Morkovsky P, Gomes JA, Kesmez M, Parga J, Cocke DL. Fundamentals, present and future perspectives of electrocoagulation. J Hazard Mater. 2004; 114: 199-210.
13. Sadaf S, Roy H, Fariha A, Rahman TU, Tasnim N, Jahan N, et al. Electrocoagulation-based wastewater treatment process and significance of anode materials for the overall improvement of the process: A critical review. J Water Process Eng. 2024; 62: 105409.
14. Yazıcı Karabulut B. Electrochemical coagulant generation via aluminum-based electrocoagulation for sustainable greywater treatment and reuse: Optimization through response surface methodology and kinetic modelling. Molecules. 2025; 30: 3779.
15. Agarwal P, Sangal VK, Mathur S. Treatment of textile effluent by electrocoagulation in a novel reactor to mitigate environmental pollution. Int J Environ Sci Technol. 2025; 22: 3393-3404.
16. Cruz FF, Góes MC, Santana CG, Santos TG, Boscolo M, Luz RC, et al. Optimizing electrocoagulation for textile effluent treatment: Operational efficiency and environmental assessment of Remazol red dye removal. ACS Omega. 2025; 10: 62962-62978.
17. Lamhar R, Kambuyi TN, Bejjany B, Kherbeche A, Digua K, Dani A. Electrocoagulation for the decolorization of textile wastewater in single-channel reactor: Response surface methodology for optimization and a novel model exploitation. J Clean Prod. 2024; 450: 141900.
18. Rezaei S, Heidarpour M, Aghakhani A, Zargoosh K. Comprehensive study on the batch electrocoagulation for real dyeing wastewater treatment. Sci Rep. 2026; 16: 9167.
19. Companhia BJ, Scalize PS. From batch to continuous in electrocoagulation: Key parameters for efficient scaling in water treatment. Environ Sci Pollut Res. 2025; 32: 22163-22193.
20. Al-Qodah Z, AL-Rajabi MM, Al Amayreh HH, Assirey E, Bani-Melhem K, Al-Shannag M. Performance of continuous electrocoagulation processes (CEPs) as an efficient approach for the treatment of industrial organic pollutants: A comprehensive review. Water. 2025; 17: 2351.

21. Al-Qodah Z, AL-Rajabi MM, Da'na E, Al-Shannag M, Bani-Melhem K, Assirey E. Continuous electrocoagulation processes for industrial inorganic pollutants removal: A critical review of performance and applications. Water. 2025; 17: 2639.
22. Hellal MS, Doma HS, Abou-Taleb EM. Techno-economic evaluation of electrocoagulation for cattle slaughterhouse wastewater treatment using aluminum electrodes in batch and continuous experiment. Sustain Environ Res. 2023; 33: 2.
23. Kuokkanen V, Kuokkanen M, Hynynen I, Kuokkanen T. Electrocoagulation treatment of metallurgical industry wastewater-A laboratory scale batch and pilot scale continuous study. Hydrometallurgy. 2021; 202: 105596.
24. Bani-Melhem K, Alnaief M, Al-Qodah Z, Al-Shannag M, Elnakar H, AlJbour N, et al. On the performance of electrocoagulation treatment of high-loaded gray water: Kinetic modeling and parameters optimization via response surface methodology. Appl Water Sci. 2025; 15: 114.
25. Soltan Y, Bani-Melhem K, Ba-Abbad M, Almomani F, Al-Muhtaseb AA. Optimization of aluminum electrocoagulation parameters for nutrient removal from hydroponic wastewater using response surface methodology. Water. 2025; 17: 3346.
26. García-Ávila F, García-Uzca C, Quizhpilema-Marín S, Salazar-Armijos MJ, Segura-Paima M, Valdiviezo-Gonzales L. Electrocoagulation for industrial wastewater remediation: Efficiency, operational optimization and sustainable implementation. J Electrochem Sci Eng. 2026; 16: 3068.
27. Dobrosz-Gómez I, Ibarra-Taquez HN, Gómez-García MÁ. Evaluation of the environmental and economic scope of an electrocoagulation process for the treatment of wastewater from the instant coffee industry. J Solid State Electrochem. 2025; 29: 3441-3463.
28. Salazar-Sogamoso LM, Gomez-Garcia MA, Dobrosz-Gomez I. Comparative life cycle assessment of sequential chemical and electrochemical processes for the treatment of industrial textile wastewater. J Solid State Electrochem. 2025; 29: 3379-3399.
29. Joag S, Kiesewetter J, Chellam S. Electrode corrosion, pH, and dissolved oxygen dynamics, and hardness/silicon removal during aluminum electrocoagulation of hypersaline produced water. ACS EST Eng. 2024; 5: 86-102.
30. Joag S, Kiesewetter J, Chellam S. Ohmic losses dominated electrode fouling during long-term aluminum electrocoagulation of hypersaline and divalent cation-rich oilfield-produced water. ACS EST Eng. 2025; 5: 3519-3532.
31. Holt PK, Barton GW, Mitchell CA. The future for electrocoagulation as a localised water treatment technology. Chemosphere. 2005; 59: 355-367.
32. Burnham KP, Anderson DR. Model selection and multimodel inference: A practical information-theoretic approach. New York, NY: Springer; 2002.
33. Syafalni S, Abustan I, Dahlan I, Wah CK, Umar G. Treatment of dye wastewater using granular activated carbon and zeolite filter. Mod Appl Sci. 2012; 6: 37-51.
34. Barnett V, Lewis T. Outliers in statistical data. 3rd ed. New York, NY: Wiley; 1994.
35. Ghasemi A, Zahediasl S. Normality tests for statistical analysis: A guide for non-statisticians. Int J Endocrinol Metab. 2012; 10: 486-489.
36. Cohen J. Statistical power analysis for the behavioral sciences. 2nd ed. New York, NY: Routledge; 1988.
37. Ortenero JR, Choi AE. Electrocoagulation treatment of wastewater: A pareto frontier identification based on the total dissolved solids and cost. Chem Eng Trans. 2022; 94: 781-786.

38. Choi AE, Ortenero JR. Fuzzy optimization for the remediation of saline oily wastewater through electrocoagulation: A multi-objective case analysis. Clean Techn Environ Policy. 2024; 26: 1621-1630.
39. Bazrafshan E, Alipour MR, Mahvi AH. Textile wastewater treatment by application of combined chemical coagulation, electrocoagulation, and adsorption processes. Desalin Water Treat. 2016; 57: 9203-9215.
40. Bener S, Bulca Ö, Palas B, Tekin G, Atalay S, Ersöz G. Electrocoagulation process for the treatment of real textile wastewater: Effect of operative conditions on the organic carbon removal and kinetic study. Process Saf Environ Prot. 2019; 129: 47-54.
41. Abdollahi J, Moghaddam MR, Habibzadeh S. Uncovering the key determinants of electrode passivation and faradaic efficiency in electrocoagulation: Depassivation and sustainable performance via polarity reversal. Environ Res. 2025; 279: 121889.
42. Syaichurrozi I, Sarto S, Sediawan WB, Hidayat M. Experiment and kinetic analysis of the effect of agitation speed on electrocoagulation process for the treatment of vinasse. J Water Process Eng. 2022; 50: 103144.
43. Indrayani L, Rahmah N. Pollutant parameter values as determinants of the treatment-stage effectiveness of batik industry wastewater [Nilai Parameter Kadar Pencemar sebagai Penentu Tingkat Efektivitas Tahapan Pengolahan Limbah Cair Industri Batik] (In Indonesian). J Rek Pros. 2018; 12: 41-50. doi: 10.22146/jrekpros.35754.
44. Putra RS, Annisa AD, Budiarjo S. Batik wastewater treatment using simultaneous process of electrocoagulation and electro-assisted phytoremediation (EAPR). Indones J Chem. 2020; 20: 1221-1229.
45. Hayden J, Abbassi B. Continuous flow electrocoagulation system for enhanced phosphorous removal in decentralized wastewater treatment systems. Water. 2025; 17: 202.